frontiers | Frontiers in Nanotechnology

REVIEW
published: 09 June 2022
doi: 10.3389/fnano.2022.827925

Potential Application of Perovskite Structure for Water Treatment: Effects of Band Gap, Band Edges, and Lifetime of Charge Carrier for Photocatalysis

J. L. Clabel H., J. Chacaliaza-Ricaldi and E. Marega Jr.*

São Carlos Institute of Physics, University of São Paulo, São Carlos, Brazil

Perovskite structures have attracted scientific interest as a promising alternative for water treatment due to their unique structural, high oxidation activity, electronic stability, and optical properties. In addition, the photocatalytic activity of perovskite structures is higher than that of many transition metal compounds. A critical property that determines the high-performance photocatalytic and optical properties is the band gap, lifetime of carrier charge, and band edges relative to the redox potential. Thus, the synthesis/processing and study of the effect on the band gap, lifetime of carrier charge, and band edges relative to the redox potential in the development of high-performance photocatalysts for water treatment are critical. This review presents the basic physical principles of optical band gaps, their band gap tunability, potentials, and limitations in the applications for the water treatment. Furthermore, it reports recent advances in the synthesis process and comparatively examines the band gap effect in the photocatalytic response. In addition to the synthesis, the physical mechanisms associated with the change in the band gap have been discussed. Finally, the conclusions of this review, along with the current challenges of perovskites for photocatalysis, are presented.

Keywords: photocatalysis, band gap, lifetime, water pollution, perovskite

OPEN ACCESS

Edited by:
Alexandre Pinto,
Manhattan College, United States

Reviewed by:
Kesong Yang,
University of California, San Diego, United States
Jun Ke,
Wuhan Institute of Technology, China

****Correspondence:***
J. L. Clabel H.
jclabel@ifsc.usp.br

Specialty section:
This article was submitted to Environmental Nanotechnology, a section of the journal Frontiers in Nanotechnology

Received: *02 December 2021*
Accepted: *14 March 2022*
Published: *09 June 2022*

Citation:
Clabel H. JL, Chacaliaza-Ricaldi J and Marega Jr. E (2022) Potential Application of Perovskite Structure for Water Treatment: Effects of Band Gap, Band Edges, and Lifetime of Charge Carrier for Photocatalysis. Front. Nanotechnol. 4:827925. doi: 10.3389/fnano.2022.827925

1 INTRODUCTION

The development of human society today diverges from preserving life's most essential natural resource, water. Water pollution is generated by different sources of industrialization, conventional fossil fuel use, and population growth (Yousif and Gurjar, 2018), which leads to an increase in demand for clean water supply. The global challenge is achieving environmental sustainability since only less than 1% of fresh water on the earth is readily accessible (Reid et al., 2019). In addition to the increase in both the volumes and the concentrations of polluted water, a decrease in biodegradability of the pollutants was observed. Such problems have created a strong incentive for the development of new sustainable and high-efficiency materials, when compared to those already existing (Patel et al., 2019; Schanze et al., 2020), aiming at the abatement of pollutants. In this context, the solar energy source (as future sustainability) is very attractive in photocatalytic materials due to their remarkable effectiveness for water treatment. Solar energy harvesting is also enjoyed in other fields as photothermal and photovoltaic. Photocatalytic materials are a rapidly growing field for potential application with clean and renewable energy sources (Belver et al., 2019; Odling and Robertson, 2019;

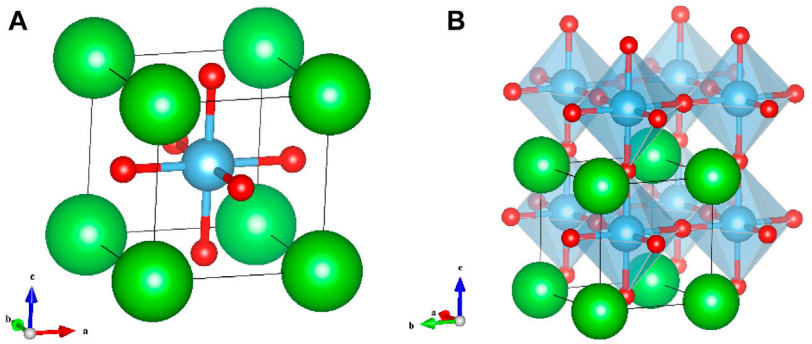

FIGURE 1 | (A) Unit cell of ABX_3 perovskite. **(B)** Crystal structure of a simple perovskite compound. Blue color (A-site), green color (B-site), and red color (X-site).

Xia et al., 2021). The photocatalytic materials absorb sunlight to produce electron (e^-) and hole (h^+) pairs, which are fundamental for environmental remediation, such as water purification (Karthikeyan et al., 2020).

Recent advances in nanostructured materials have opened the way for new types of semiconductor catalysts and improving TiO_2 or ZnO for the destruction of polluting materials (Roy and Chakraborty, 2021; Chen et al., 2020a). Among the various classes of materials explored, perovskite (ABX_3) has been given much interest due to its framework's easiness and versatility, excellent photostability, and photocatalytic nature (Zhang et al., 2016; Hwang et al., 2017), and its structural integrity representation is shown in **Figure 1**. The A-site ions are generally rare or alkaline earth elements (often occupied by a larger-size cation), B-site ions are usually transitioned metal elements (occupied by a smaller cation), and X is often a chalcogen or halogen. The advantage of perovskite structures is that they can incorporate a wide variety of ions of various sizes and charges showing great flexibility of composition; besides, their crystal structure can remain unchanged (Tasleem and Tahir, 2020). However, most perovskites are usually distorted. The partial substitution of these cations, both A-site and B-site ions, by other foreign ions leads to changes in the oxidation states of metal ions. The B-site substitution can result in the double perovskite formula ($A_2BB'X_6$).

Furthermore, the substitutions are accompanied by the formation of intrinsic defects due to the mechanism of charge compensation (Liu et al., 2020a). Kurbakov (2010) stated that replacing an A^{3+} with A^{2+} results in lattice distortion and the formation of oxygen vacancies. Golsdschmidt (1962) proposed that the formation of a perovskite structure can be governed by a tolerance factor, which predicts the stability and distortion of the perovskite structure, as follows: $t = (r_A + r_B)/[\sqrt{2}(r_B + r_X)]$, where r_A, r_B, and r_X are ionic radii of each ion (A, B, and X). The tolerance factor assesses whether the A-site cation can fit within the cavities in the BX_3 framework. Although the information of stability using t is essential for the prediction of perovskite stability by Goldschmidt, it has recently been shown that its accuracy is often insufficient (Bartel et al., 2019). Recently, Bartel et al. (2019) suggested a new tolerance factor (τ) to

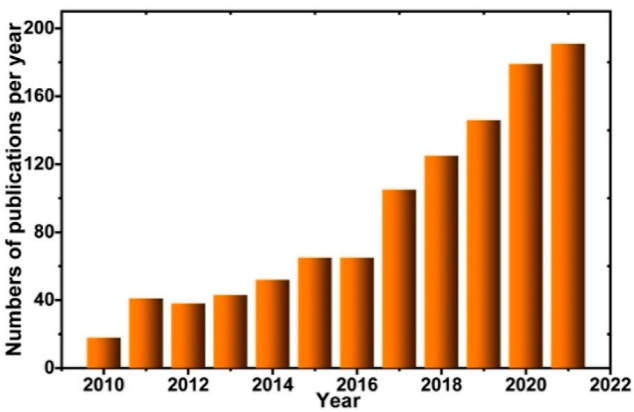

FIGURE 2 | Number of publications per year and the cumulative number of publications on perovskites and photocatalysis from 2010 to 2021 from Scopus with work: perovskite and photocatalysis.

predict the stability of perovskite oxides and halides, which has the following form:

$$\tau = \frac{r_X}{r_B} - n_A\left(n_A - \frac{r_A/r_B}{ln(r_A/r_B)}\right), \quad (1)$$

where n_A is the oxidation state of A, $r_A > r_B$, and $\tau < 4.18$ indicates perovskite. The calculations determine a better accuracy of τ, for example, for oxides of 83–92% and halides (chlorides) of 51–90%.

The formation of single and double perovskite materials has exceptional properties for a variety of applications such as ferroelectricity (Cohen, 1992), ferromagnetism (Clabel H. et al., 2016), multiferroic (Clabel H. et al., 2014), electrocatalysis (Hwang et al., 2017), optical (Clabel H. et al., 2017), and photocatalytic (Grabowska, 2016), among others (Kovalenko et al., 2017; Correa-Baena et al., 2017). Due to its application potential, researchers have made extensive efforts on perovskite material as a photocatalyst. As shown in **Figure 2**, an upward trend of the number of publications based on perovskite photocatalysts was observed from 2010 to 2021. Although there is growing research into perovskites for photocatalytic applications,

there are still inherent limitations associated with the following: 1) the wide band gap (E_g) renders only ultraviolet spectra absorption; 2) particle size; 3) low surface area, which limits the reactant to adsorbing on the surface; 4) high degree of recombination of photoinduced charges ($e^- - h^+$) that have limited their efficiency in the photocatalytic reactivity for water treatment (Modak et al., 2014; Chen et al., 2020b); and 5) short luminescence lifetime, which limits the charge separation efficiency. These factors lead to different strategies in order to overcome such shortcomings as synthesis method, composition, and doping. Notwithstanding these limitations being important, the intrinsic property that is more relevant is the wide band gap (>3.0 eV) due to which they can be activated under ultraviolet light (Kumar et al., 2020). In this sense, the band gap should be tunable in the perovskite structure, in order to find a suitable E_g to utilize visible light fully and effectively, which is a current challenge.

In this review, many single perovskite compounds have been reported to be photocatalysts for water treatment. We discuss the perovskite structures that have been considered, their properties, and current synthesis methods to form oxide and halide perovskites. Following this, we have summarized the recent reports addressing the influence of band gap and lifetime of charge carrier of perovskite structure in photocatalytic activity efficiency for water treatment. Factors associated with the tunable band gap will be discussed. Finally, a summary of the recent advances in perovskite photocatalysts will be given.

2 SYNTHESIS METHODS OF THE PEROVSKITE PARTICLES

Among the strategies adopted in optimizing photocatalysts, the synthesis methods greatly impact their physical properties. Several strategies were developed to adjust the particle size, surface area, shape, and composition to optimize the photocatalytic process. The photocatalytic activity of perovskite structure dramatically depends upon the specific surface area and band gap as well. The high surface area provides enough reaction sites and improves the adsorption properties of the photocatalysts; furthermore, an appropriate band gap allows for tuning the absorption of a particular wavelength region of light. Thus, the relevance in the synthesis methods is significant in the photocatalytic performance for water treatment.

2.1 Solid-State Reaction

Synthesis by solid-state reactions (SSRs) results in a mixture of nitrates, carbonates, acetate, and oxides, with desired stoichiometric ratios. Perovskites are frequently synthetized by SSRs, including mixing, milling, and calcination at high temperatures to form the perovskite phase. During this process, surface chemical defect and particle size effects affect the process of recombination of photoinduced charge carriers ($e^- - h^+$), which limits their efficiency in photocatalytic reactivity (Chen and Ye, 2007). However, it was shown that the milling time in ball milling (see **Figure 3**) and the solvent change the particle size and functional group absorption, this last owing to the active site generated on the particle surface (Clabel H et al., 2020). Such factors modified the optical properties of the perovskite structure (Clabel H. et al., 2021a). Also, the high energy transferred by the impacts during ball milling and calcination allowed single phases (Protesescu et al., 2018; Clabel H et al., 2020).

2.2 Sol-Gel

Perovskite structure synthesized by sol-gel method involves the formation of a sol by dissolving the metal alkoxide, metal-organic, or metal-inorganic salt precursors in a suitable solvent, which is subsequently condensed to form a gel, followed by pre-calcination (removal of organic material) and calcination at much lower temperatures than those of the solid-state reaction for the formation of perovskite structure. Some frequently used gels include ethanol, ammonia, polyvinyl alcohol, and citric acid, among others. Furthermore, used precursors, the pH value, and the heat treatment schedule play an essential role in affecting the properties of the perovskite structure (Brutchey and Morse, 2006; Ismael and Wark, 2019).

2.3 Hydrothermal and Solvothermal

Hydrothermal and solvothermal methods require heating an aqueous suspension of insoluble salts, that is, reaction mixture, in an autoclave at high temperature and pressure conditions where the crystallization of the desired phase is taking place. The product generates perovskite powders with high crystallinity and purity, low concentration of defects, and controllable size distribution and morphologies. High photocatalytic activity in $KNbO_3$ materials for H_2 evolution from aqueous CH_3OH solutions was reported for high surface area and crystallinity (Ding et al., 2008). In perovskites of Cr-doped $SrTiO_3$, high surface area (19.3–65.4 $m^2\,g^{-1}$), good crystallinity, and small crystalline size (20–30 nm) were obtained using a sol-gel hydrothermal method (Yu et al., 2011). Solvothermal synthesis of $BaTiO_3$, $PbTiO_3$, $SrTiO_3$, and $BaZrO_3$ leads to particles with different morphologies (Caruntu et al., 2015). The characteristic of perovskite powders with unique optical properties makes the method advantageous in optimizing photocatalysts.

2.4 Co-Precipitation

In the co-precipitation method, the starting materials used have been taken in stoichiometric proportions in molar solutions. These are denominated precursors such as metal acetate, sulfates, chloride, or nitrate. Afterward, the solutions have been poured into a precipitant solution (e.g., NaOH or Na_2CO_3) under constant stirring. In this step, the nucleation process forms a large number of small particles, and then the post nucleation process and Ostwald ripening and aggregation dramatically affect the product size, morphology, and properties. During co-precipitation, the pH value of the solution has been controlled. Precipitation takes place in the solution at a determined temperature (>70°C), in which the supersaturation conditions help to induce precipitation as the result of a chemical reaction (Chang Chien et al., 2022). The precipitates are collected and washed several times and then dried in a hot air oven at a temperature >70°C. The advantages of this

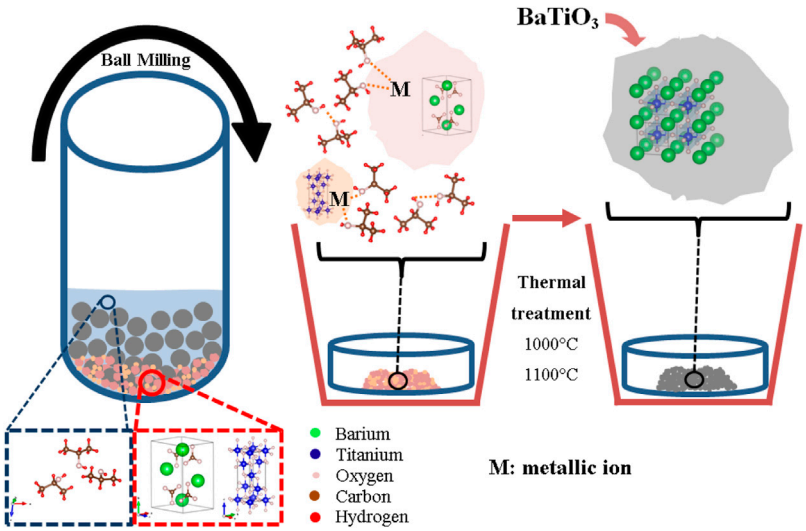

FIGURE 3 | Schematic views of the synthesis process by solid-state reaction to prepare nanopowders of $BaTiO_3$ (Clabel H et al., 2020).

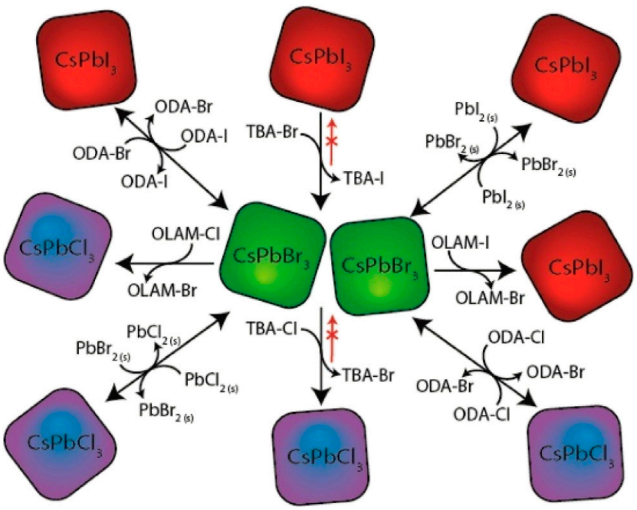

FIGURE 4 | Schematic views of the different routes and precursors for the anion exchange reactions on CsPbX3 (X = Cl, Br, I) nanocrystals (Akkerman et al., 2015).

method are the high yield, high product purity, the lack of necessity to use organic solvents, easy reproducibility, and low cost (Letifi et al., 2021). However, the properties of the obtained particles, such as size, shape, and composition, are highly dependent on the reaction parameters such as temperature, pH, and ionic strength (Haron et al., 2018). Furthermore, co-precipitation is also a more straightforward method; however, it is not stable and hence is stabilized by using a surfactant.

2.5 *In Situ* Anion Exchange Reaction

This method was demonstrated to be an effective strategy to synthesize nanocrystals with engineered compositions and structures (Fenton et al., 2018). Also, it has attracted increasing attention in the fabrication of heterostructure photocatalysts to improve photocatalytic performance. The ion-exchange reaction is normally performed in molten salt or solvothermal conditions. Heating to a high temperature (e.g., 300°C or above) is needed in the former case, often leading to decomposition of the material or the formation of a more stable structure. Using ion-exchange reactions under mild solvothermal conditions would be preferable in many cases, wherein the reaction is performed at the lowest possible temperature (below 200°C) sufficient to accelerate exchange kinetics (Park et al., 2017). Different perovskites by anion exchange reaction (see **Figure 4**) were mentioned in the literature showing enhanced photocatalytic properties, like $CsPbX_3$ (X = Cl, Br, I) (Akkerman et al., 2015; Loiudice et al., 2019), Cs_2AgBiX_6, (X = Cl or Br) (Creutz et al., 2018), and Cs_2AgBiX_6 (X = Cl, $Cl_{0.5}Br_{0.5}$, Br, $Br_{0.5}I_{0.5}$, I) (Wu et al., 2021).

3 PEROVSKITE STRUCTURE IN PHOTOCATALYSIS

Human activity and industrialization growth lead to environmental pollution, especially clean water reduction. Thus, perovskite structures based on the crystal structure, physical properties, and their strategies help degrade pollutants, which are highly active in the presence of ultraviolet (UV) energy radiations but weakly active in visible (vis) and near-visible (NIR) light. On the other hand, in addition to the new tolerance factor τ, geometry consideration is another essential structure parameter in halide perovskites, called octahedral factor μ, defined as follows (Li et al., 2008):

$$\mu = \frac{r_B}{r_X}. \tag{2}$$

TABLE 1 | ABX_3-based photocatalysts.

Perovskite	Synthesis method	Light source	Indicator of pollutants	Reference
Perovskite oxide				
$BaTiO_3$	Sol-gel	UV–vis	Diclofop-methyl	Gomathi Devi and Krishnamurthy, (2009)
$BaTiO_3$	Solid-state reaction	UV light	Blue Rz ink (Resazurin)	Kumar et al. (2019)
$BaTiO_3$	Hydrothermal	UV light	Methyl orange	Liu et al. (2020b)
$SrTiO_3$	Sol-gel	UV–vis	Methylene blue	Hsieh et al. (2019)
$SrTiO_3$	Microwave-assisted hydrothermal	UV light	Rhodamine B	Da Silva et al. (2013)
$CaSnO_3$	Co-precipitation	UV light	4-Nitrophenol	Gómez-Solís et al. (2019)
$BaSnO_3$	Co-precipitation	UV light	4-Nitrophenol	Gómez-Solís et al. (2019)
$SrSnO_3$	Co-precipitation	UV light	4-Nitrophenol	Gómez-Solís et al. (2019)
$CaTiO_3$	Hydrothermal	UV–vis	Rhodamine B	Yan et al. (2018)
$BiFeO_3$	Hydrothermal	Visible light	Methyl orange	Chen et al. (2017)
$LaFeO_3$	Sol-gel auto-combustion	Visible light	—	Parida et al. (2010)
$LaNiO_3$	Microemulsion	Visible light	Rhodamine B	Ghafoor et al. (2021)
$KNbO_3$	Hydrothermal	Visible light	Rhodamine B, orange G, bisphenol A, and pentachlorophenol	Wang et al. (2013)
$NaTaO_3$	Molten salt method	UV light	Rhodamine B (5 mg/L)	Wang et al. (2017a)
$NaTaO_3$	Solid-state reaction	Visible light	—	Kanhere et al. (2012)
$NaTiO_3$	Solvothermal	Visible light	NO_x gas	Wu et al. (2013)
$KTaO_3$	Solvothermal	Visible light	Methylene blue	Rao et al. (2018)
$BaZrO_3$	Solvothermal	UV light	—	Meng et al. (2019)
$LaMnO_3$	Biotemplate	UV–vis	Methylene blue	Wang et al. (2019)
$LaMnO_3$	Sol-gel	UV–vis	Methyl orange	Rekavandi et al. (2019)
$LaMnO_3$	Sol-gel	—	—	Ibarra-Rodriguez et al. (2020)
$LaFeO_3$	Sol-gel	—	—	Ibarra-Rodriguez et al. (2020)
$LaCoO_3$	Sol-gel	—	—	Ibarra-Rodriguez et al. (2020)
$SrSnO_3$	Microwave	UV light	Methanol	Alammar et al. (2017)
$LiTaO_3$	Hydrothermal	—	—	Takasugi et al. (2015)
$LiTaO_3$	Solvothermal	—	—	Takasugi et al. (2015)
Doped-perovskite oxide				
$La_{0.7}Sr_{0.3}MnO_3$	Citrate method	Sunlight	Methyl orange (13 ppm)	Ghiasi and Malekzadeh, (2014)
$La_{0.5}Sr_{0.5}FeO_3$	Sol-gel	UV light	2,4-Dichlorophenoxyacetic acid (2,4-D)	Cheng et al. (2020)
$La_{0.4}Sr_{0.6}MnO_{3-\delta}$	Sol-gel	UV light	Phenol	Miao et al. (2019)
$LaCo_{0.4}Mn_{0.6}O_3$	Sol-gel	Sunlight	Phenol	Lu et al. (2018)
$LaTi_{0.4}Cu_{0.6}O_3$	Sol-gel	UV light	Rhodamine B	Zhang et al. (2012)
$BiFe_{1-x}Mn_xO_3$	Sol-gel	UV light	Bisphenol A	Soltani et al. (2018)
$SrCo_{0.9}Ti_{0.1}O_{3-\delta}$ $SrCo_{0.8}Ti_{0.2}O_{3-\delta}$ $SrCo_{0.6}Ti_{0.4}O_{3-\delta}$ $SrCo_{0.4}Ti_{0.6}O_{3-\delta}$	Sol-gel	—	Phenol	Miao et al. (2017)
$La_{0.95}Gd_{0.05}Ni_{0.9}Co_{0.05}Fe_{0.05}O_3$	Microemulsion	Visible light	Rhodamine B	Ghafoor et al. (2021)
$La_{0.90}Gd_{0.10}Ni_{0.8}Co_{0.10}Fe_{0.10}O_3$				
$La_{0.85}Gd_{0.15}Ni_{0.7}Co_{0.15}Fe_{0.15}O_3$				
$La_{0.80}Gd_{0.20}Ni_{0.6}Co_{0.20}Fe_{0.20}O_3$				
$La_{0.75}Gd_{0.25}Ni_{0.5}Co_{0.25}Fe_{0.25}O_3$				
$BiFeO_3:Gd^{3+}$	Sol-gel	UV light		
$Ba_{0.8}Sr_{0.2}TiO_3$	Sol-gel	UV light	—	Liu et al. (2021)
$Ba_{0.7}Sr_{0.3}TiO_3$				
$Ba_{0.6}Sr_{0.4}TiO_3$				
$Ba_{0.5}Sr_{0.5}TiO_3$				

The μ value describes the stability of BX_6 octahedra. This octahedral factor combined with its chemical nature is essential to predict the stability of perovskites, in addition to τ. The doping at both A and B sites with other elements results in compositional and symmetry changes. The compensation charge gives rise to the formation of chemical defects, thus modifying the electronic, light absorption, adsorption, and photocatalytic properties of the perovskite structure. As a strategy to the high efficiency of perovskites applied in photocatalysis, the doping in perovskites is frequently adopted, owing to that can tune the band gap and hence the optical properties of the perovskite structure. Others strategies are as follows: control particle size, porosity, synthesis method, treatment in gas flux, and surface area were considered in order to enhance the photocatalytic activity. Several systems

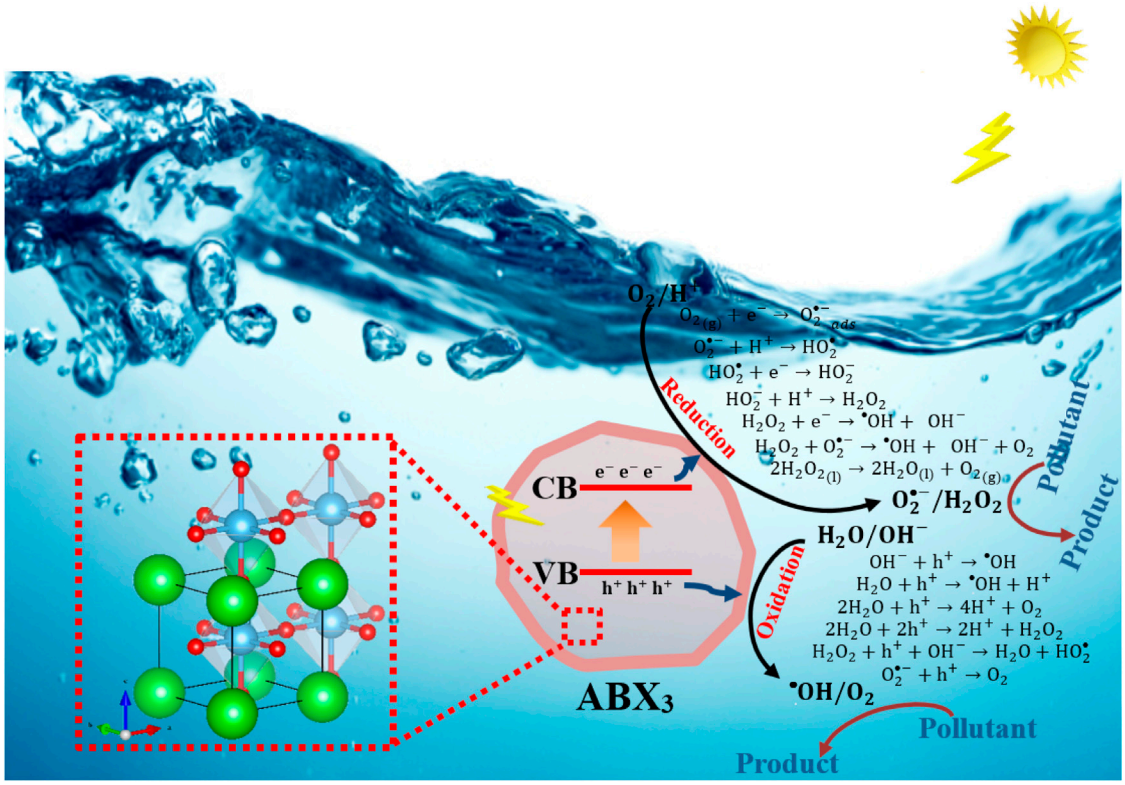

FIGURE 5 | Schematic representation of the band structure and mechanism of photogenerated charge carrier transfer to photocatalytic reaction on perovskites.

mainly focused on perovskite structure were applied to photocatalytic property; a summary is exhibited in **Table 1**. To know the effectiveness of photocatalysts, numerous organic pollutants have been utilized as model contaminants, such as methylene blue, rhodamine B, methyl orange, 4-chlorophenol, and 4-nitrophenol (see **Table 1**).

4 PHOTOCATALYTIC MECHANISM

Understanding the source of solar energy irradiation is the first step when enhancing the optical properties and, consequently, photocatalytic activity. Photocatalytic activity from solar energy has become an essential topic in the scientific community to solve the polluted water problem and eliminate pollutants in natural aquatic systems. In this sense, the solar energy irradiation contributed with different ultraviolet (UV), visible (VIS), and near-infrared (NIR) bands. The solar energy irradiation is lower in the UV band, at 3.4%. The solar energy irradiation in the VIS band understands a fraction at 42%. The most considerable portion of total solar energy irradiation occurs in the NIR band, at 54.6%. Solar-driven photocatalyst involves the generation of active oxidizing species under solar irradiation, in the presence of a catalyst, as a perovskite structure. A suitable band gap and high photoinduced charge separation efficiency are critical factors for ideal photocatalysts. A severe limitation of most photocatalysts is that they can only absorb photons with light wavelengths <400 nm (UV band), which accounts for 3.4% of the total solar energy irradiation. As described before, solar energy irradiation in the VIS band is high, so the development and optimization of photocatalysts with high efficiency and chemical stability in the VIS band will favor the photocatalytic reaction processes.

Different pathways characterize the photocatalytic process, and they are described as follows:

(i) photons with higher energy ($h\nu$), of the solar energy irradiation, are absorbed by a photocatalyst with energy matches or higher than the band gap energy (E_g);
(ii) subsequently, the electrons (e^-) are excited from the VB to the CB, giving rise to the holes (h^+) in the CB and $e^- - h^+$ generation; the excited electrons and holes can either undergo direct recombination or diffuse separately and migrate to the surface of the particles or are trapped by the defects in the bulk material; and
(iii) the production electron (e^-)-hole (h^+) pairs initiate and enhance the degradation process of the catalyst for the pollutant's treatment through the photo-assisted redox reaction. In this process, the e^- and h^+ on the active sites of the photocatalyst surface act as reducing and oxidizing agents (Hoffmann et al., 1995).

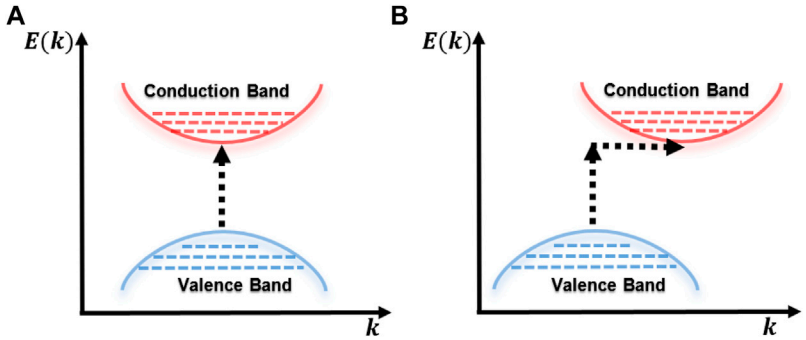

FIGURE 6 | Diagram of band–band transitions. **(A)** Direct. **(B)** Indirect.

TABLE 2 | Values of r for band–band transitions.

Transition type	Allowed	Forbidden
Direct	1/2	1/3
Indirect	2	3

The photocatalytic activity depends on the generation and the separation of $e^- - h^+$ pairs. In step (ii), the h^+ generation can combine or react with adsorbed H_2O molecules or OH^- group to form hydroxyl radical ($^{\bullet}OH$) and O_2. $^{\bullet}OH$ is a powerful oxidizing agent and attacks organic molecules. In the presence of dissolved O_2, the CB e^- can react with O_2 and H^+ to form the superoxide radical ($O_2^{\bullet -}$) and hydrogen peroxide (H_2O_2); this process is shown in **Figure 5**. The $O_2^{\bullet -}$ also react with a proton to form hydroperoxyl radical ($^{\bullet}OOH$), which is responsible for the formation of hydrogen peroxide (H_2O_2). Subsequently, the dissociation of H_2O_2 again generates highly reactive $^{\bullet}OH$ (Hoffmann et al., 1995; Peoples et al., 2019). Furthermore, the $e^- - h^+$ pair recombination density reduced the supply of charge carriers (electrons and holes) adsorbed to the catalyst surface for reduction and/or oxidation reactions (redox). This can be explained as follows: when e^- in the CB falls into h^+ in the VB ($e^- - h^+$ recombination), free e^- and h^+ are eliminated, which leads to dissipation of the input energy in the form of heat or emitted light. Consequently, the redox reactions are reduced. In order to limit the $e^- - h^+$ in recombination processes, co-catalysts such as Pt, Pd, NiO, and RuO_2 are applied to the particle surface.

In addition to the limitation mentioned above for photocatalyst application, other factors can influence photocatalytic activity, as described in the following section. An efficient photocatalyst should contain the following: 1) a band gap ≥1.2 eV to provide energetic electrons and a band gap ≤3.0 eV to allow effective absorption of overlap with the solar spectrum and 2) a high surface area to optimize the redox reaction and minimize the recombination process.

4.1 Band Gaps in Perovskite Materials

In condensed matter physics, the band gap energy is an energy region where the electronic states cannot exist. It separates the upper part of the valence band from the lower part of the conduction band and characterizes the electronic properties of the solids depending on the magnitude of this separation (measured in eV). One way to calculate band gaps from experimental data for nanostructured semiconductor materials, such as perovskites, is through the model proposed by Tauc (Tauc and Menth, 1972), who performed the analysis of the incident photon energy $h\nu$ and the absorption coefficient α in the following expression:

$$\alpha h\nu = A(h\nu - E_i)^r, \tag{3}$$

where coefficient A is a proportionality constant that depends on the electronic transition probability, E_i is the edge of the optical band, and r is a real number, which depends on the type of band–band transition, as seen in **Table 2**, which indicates whether the transition is allowed or forbidden.

For direct transitions, the values of r are 1/2 and 3/2 for the allowed and forbidden processes, respectively, while for indirect transitions, the values of r are 2 and 3 for the allowed and forbidden processes, respectively (Mott, 1968).

So, materials with allowed band–band transitions can classify these transitions into two types: 1) direct transition, where the minimum energy state of the conduction band and the maximum energy state of the valence band are aligned with each other, that is, they have the same value of momentum k in the Brillouin zone, and 2) indirect transition, where the respective minimum and maximum energy states of the conduction and valence bands are misaligned, for example, due to the contribution of the phonons of the lattice (Zanatta, 2019), as can be seen in **Figure 6**.

Perovskites have unique optical properties related to a particle size such as high quantum yield, ionic conductivity, tunable composition-dependent luminescence throughout the visible region, multiphoton absorption and corresponding stimulated emission spectra, and good quantum confinement, which are essential in the field of light-active photocatalyst design because many materials are only active in the UV region (4%), so the use of nanostructured perovskites is essential because visible light occupies 45% of the spectrum of sunlight due to its wide band gap. Photocatalysts with a suitable band gap absorb sunlight,

TABLE 3 | ABX_3-based photocatalysts for water treatment.

Perovskite	Synthesis method	E_g (eV)	Surface area (m^2/g)	Pore diameter (nm)	Particle size (nm)	Reference
Perovskite oxide						
$BaTiO_3$	Sol-gel	3.33	9.64	10.49	85–286	Gomathi Devi and Krishnamurthy (2009)
$BaTiO_3$	Solid-state reaction	—	—	—	50	Kumar et al. (2019)
$BaTiO_3$	Hydrothermal		18.24	17.49	[a]	Liu et al. (2020b)
$BaTiO_3$	Solid-state reaction	2.42	—	—	990 (2[b])	Clabel H et al. (2020), Clabel H. et al. (2021a)
		2.78	—	—	370 (12[b])	
		3.58	—	—	240 (24[b])	
		2.78	—	—	1,230 (2[#])	
		2.34	—	—	440 (12[#])	
		2.43	—	—	360 (24[#])	
$BaTiO_3$	Sol-gel	3.0	—	—	23 (650°C)	Ramakanth and James Raju (2014)
		3.08	—	—	31 (700°C)	
		3.2	—	—	34 (750°C)	
		2.53	—	—	54 (800°C)	
$SrTiO_3$	Sol-gel hydrothermal	3.2	4.5	4.0	30	Yu et al. (2011)
$SrTiO_3$	Sol-gel	3.258 3.244	—	—	160	Hsieh et al. (2019)
		3.231 3.227			200 250 290	
		3.254[c]	—	—	164	
		3.158[d]	—	—	181	
		3.151[e]	—	—	168	
$SrTiO_3$	Microwave-assisted hydrothermal	3.7	27.5	<10	500	Da Silva et al. (2013)
$CaSnO_3$	Co-precipitation	3.8	2.98	—	~73 and ~197	Gómez-Solís et al. (2019)
$BaSnO_3$	Co-precipitation	3.1	53.86	—	~56 and ~213	Gómez-Solís et al. (2019)
$SrSnO_3$	Co-precipitation	4.22	2.08	—	~68 and ~288	Gómez-Solís et al. (2019)
$CaTiO_3$	Hydrothermal	3.41	4.88	2	300–500	Yan et al. (2018)
$BiFeO_3$	Hydrothermal	2.17	-	-	20	Chen et al. (2017)
$LaFeO_3$	Sol-gel auto-combustion	2.11	25.8	—	24 (500°C)	Parida et al. (2010)
		2.10	22.55	—	28 (600°C)	
		2.09	20.04	—	65.7 (700°C)	
		2.08	8.5	—	79.1 (800°C)	
		2.07	5.8	—	104.1 (900°C)	
$LaNiO_3$	Microemulsion	3.01	—	—	64.83	Ghafoor et al. (2021)
$KNbO_3$	Hydrothermal	3.22	3.92	—	90–230	Wang et al. (2013)
$NaTaO_3$	Molten salt	3.97	—	—	20–50	Wang et al. (2017a)
$NaTaO_3$	Solid-state reaction	4.01	1.13	-	200–800	Kanhere et al. (2012)
$NaTaO_3$	Solvothermal	3.82	10.07	—	—	Wu et al. (2013)
$KTaO_3$	Solvothermal	3.53	—	—	100	Rao et al. (2018)
BaZrO3	Solvothermal	4.9	9.72	3.40	200	Meng et al. (2019)
$LaMnO_3$	Biotemplate	1.7	30.3	23	<500	Wang et al. (2019)
$LaMnO_3$	Sol-gel	2.2	—	—	20	Rekavandi et al. (2019)
$LaMnO_3$	Sol-gel	1.82	26	—	100–300	Ibarra-Rodriguez et al. (2020)
$LaFeO_3$	Sol-gel	2.43	19	—	1,500–2000	Ibarra-Rodriguez et al. (2020)
$LaCoO_3$	Sol-gel	1.75	16	—	80–200	Ibarra-Rodriguez et al. (2020)
$SrSnO_3$	Microwave	3.90	10.28	3.23	53.2	Alammar et al. (2017)
$LiTaO_3$	Hydrothermal	~4.5	1.8	—	500–3,000	Takasugi et al. (2015)
$LiTaO_3$	Solvothermal	~4.0	23.7	—	10–30	Takasugi et al. (2015)
$BiFeO_3$	Sol-gel	2.28	—	—	~135	Yang et al. (2019)
Doped-perovskite oxide						
$La_{0.7}Sr_{0.3}MnO_3$	Citrate	1.6	—	—	21	Ghiasi and Malekzadeh (2014)
$La_{0.5}Sr_{0.5}FeO_3$	Sol-gel	—	—	—	50	Cheng et al. (2020)
$La_{0.4}Sr_{0.6}MnO_{3-\delta}$	Sol-gel	—	5.1	—	150	Miao et al. (2019)
$LaCo_{0.4}Mn_{0.6}O_3$	Sol-gel	—	50.9	17.6	~40	Lu et al. (2018)
$LaTi_{0.4}Cu_{0.6}O_3$	Sol-gel	—	8.5	—	38.2	Zhang et al. (2012)
$BiFe_{0.95}Mn_{0.05}O_3$	Sol-gel	1.98	—	—	20–50	Soltani et al. (2018)
$BiFe_{0.90}Mn_{0.1}O_3$		1.89			20–50	
$SrCo_{0.9}Ti_{0.1}O_{3-\delta}$ $SrCo_{0.8}Ti_{0.2}O_{3-\delta}$	Sol-gel	—	0.4	—	10–20	Miao et al. (2017)

(Continued on following page)

TABLE 3 | (*Continued*) ABX_3-based photocatalysts for water treatment.

Perovskite oxide						
Perovskite	**Synthesis method**	**E_g (eV)**	**Surface area (m^2/g)**	**Pore diameter (nm)**	**Particle size (nm)**	**Reference**
$SrCo_{0.6}Ti_{0.4}O_{3-\delta}$ $SrCo_{0.4}Ti_{0.6}O_{3-\delta}$		—	0.5	—		
		—	0.9	—		
		—	1.2	—		
$La_{0.95}Gd_{0.05}Ni_{0.9}Co_{0.05}Fe_{0.05}O_3$	Microemulsion	2.90	—	—	59.24	Ghafoor et al. (2021)
$La_{0.90}Gd_{0.10}Ni_{0.8}Co_{0.10}Fe_{0.10}O_3$		2.85	—	—	62.40	
$La_{0.85}Gd_{0.15}Ni_{0.7}Co_{0.15}Fe_{0.15}O_3$		2.76	—	—	52.63	
$La_{0.80}Gd_{0.20}Ni_{0.6}Co_{0.20}Fe_{0.20}O_3$		2.52	—	—	48.09	
$La_{0.75}Gd_{0.25}Ni_{0.5}Co_{0.25}Fe_{0.25}O_3$		2.43	—	—	53.11	
$Ba_{0.8}Sr_{0.2}TiO_3$	Sol-gel	3.049	—	—	342	Liu et al. (2021)
$Ba_{0.7}Sr_{0.3}TiO_3$		3.027	—	—	250	
$Ba_{0.6}Sr_{0.4}TiO_3$		3.044	—	—	278	
$Ba_{0.5}Sr_{0.5}TiO_3$		3.069	—	—	222	
$BiFeO_3$:Gd^{3+}	Sol-gel	2.17			~135	Yang et al. (2019)

[a]*Nanowires.*
[b]*Milling time (h) at 1000°C, # Milling time (h) at 1100°C.*
[c]*Cubes.*
[d]*Truncated cubes.*
[e]*Truncated RD.*

which produces an electronic transition from the conduction band to the valence band, leaving a hole in the first band; then, the photoinduced charge carriers separate and transfer reaction sites for, finally, the oxidation and reduction reactions to occur at the reaction sites. To increase photocatalytic efficiency, wide band gaps with adequate energy levels must be obtained (Liang et al., 2020; Xiao et al., 2020). The scaling influences the band gap value of nanostructured perovskite photocatalysts due to quantum confinement (Ou et al., 2019); other factors that also alter the perovskite band gap, in addition to size, are shape, defects, and doping, which we will discuss next.

4.1.1 Size Particle Effect on Band Gap

It is known that the nanostructuring of materials influences the physical properties of solids, and this is not alien to perovskites. The catalytic properties of perovskites depend on the size; this phenomenon is called the size effect and is fundamental in photocatalytic reactions (Hoshina, 2013), although other properties are also affected (Liu et al., 2017; Clabel H. et al., 2019; Clabel H. et al., 2021b). The band gap is a parameter key in photocatalytic reactions influenced by the particle size. The size-dependent band gap has been carried by many experimental and theoretical researchers (Schilling et al., 2018; Liu et al., 2019). Among the different characteristics in the perovskite structure is the band gap variation (Eg) with the particle size change. Size-dependent band gap of particles with perovskite structure is a well-known and studied quantum confinement effect (Efros, 1982).

Physical–chemical variables can affect the particle size, such as 1) synthesis method, 2) thermal treatment, 3) phases ratio, 4) mechanical property, 5) type bonding utilized, 6) milling time, and 7) concentration of dopant (Li et al., 2019; Liu et al., 2021). In nanoscale materials, the bands are formed by almost discrete energy levels; this is due to the confinement of a smaller size of the particle that also groups together a small number of atoms, thus decreasing the superposition of energy levels, so there is an increase in the separation between bands. Then, the confinement of the electrons within the atoms means the limitation of their movement to a space with dimensions of the de Broglie wavelength, and then they will present a lower electrical conductivity (Pellegrini et al., 2005; Li and Li, 2006).

Liu et al. (2021) reported an analysis of the relationship between band gap energy and the Ba:Sr relationship in the $Ba_{1-x}Sr_xTiO_3$ synthesized using the sol-gel method. **Table 3** shows that the band gap increases as the grain size decreases; the lowest band gap energy is 3.027 eV, corresponding to the 7:3 ratio, which has more effective use of sunlight due to the lowest band gap of nanoparticles and absorption of visible light at wavelengths less than 409.6 nm, which promotes a higher photocatalytic hydrogen production rate. On the other hand, Ramakanth and James Raju (2014) calculated the band gap using the Tauc plot of $BaTiO_3$ nanoparticles synthesized using the sol-gel method at different calcination temperatures, as shown in **Table 3**.

Furthermore, other types of morphology are also dependent on size, as revealed by Oksenberg et al. (2020), and they show the lattice distortions and size-dependent band gap in $CsPbBr_3$ perovskite nanowires. They will identify that the contribution to the band gap modulation is height-dependent on the nanowire. In the excitation configuration, the emission spectra blue-shift with decreasing height (thickness) of the nanowires, and such shift reflects the ability of the nanowires to absorb light of different wavelengths. Thus, thinner nanowires have higher band gap energies than thicker nanowires. With decreasing nanowire heights from ~400 to ~100 nm, a significant emission blue-shift from ~525 to ~490 nm (~2.36–~2.53 eV) was observed. On the other hand, Pei-Lun et al. (Hsieh et al., 2019) explored the effects of the particle size distribution and faces on the charge carrier dynamics and the photocatalytic activity in $SrTiO_3$ cubes. The cube's size affects the band gap,

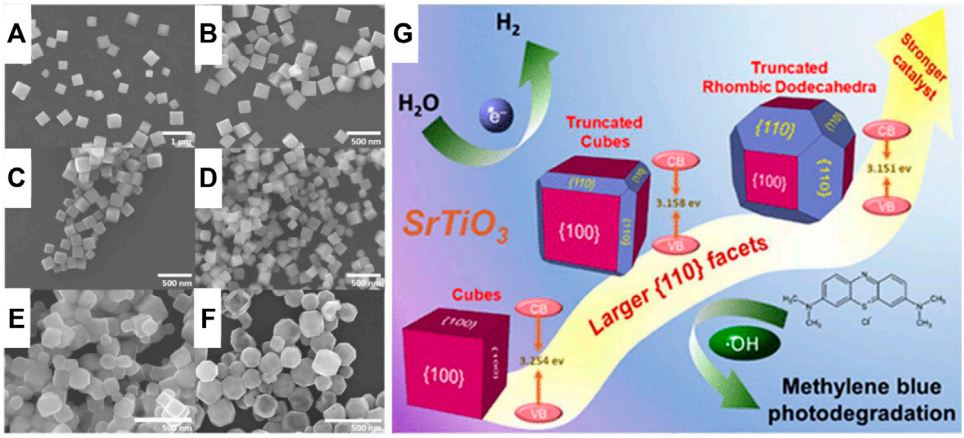

FIGURE 7 | SEM images of the synthesized $SrTiO_3$ cubes with tunable edge lengths of **(A)** 290 nm, **(B)** 250 nm, **(C)** 200 nm, and **(D)** 160 nm, **(E)** edge-truncated cubes, **(F)** {100}-truncated rhombic dodecahedra, and **(G)** The cubes display slight size-related optical band shifts, and they show clearly more blue-shifted light absorption than the other particles exposing significant {110} faces. These factors lead to a high photocatalytic activity (Hsieh et al., 2019).

showing more blue-shifted light absorption than the other particles exposing significant {110} faces. However, lattice distortion in the corners of the {100}-truncated rhombic dodecahedra are far more efficient than cubes at photodegradation of methylene blue and photocatalyzed hydrogen evolution from water in the presence of methanol, as shown in **Figure 7G**. Therefore, the photocatalytic reaction depends on particle size and faces of $SrTiO_3$, suggesting surface facet control as a strategy for enhancing photocatalyzed hydrogen production. Clabel H et al. (2020) showed that the milling time and calcination temperature modified the band gap; in addition, a lattice strain was observed, caused both by milling time and calcination. In this sense, light absorption and slight shift enhancement can be associated with strain, particle size, and chemical defects in their surface (Clabel H et al., 2020). Also, the particle strain is most likely caused by lattice defects. These lattice defects can act as traps for photoexcited electrons and holes, leading to a decrease in the efficiency of the photocatalyst. Therefore, the small values of strains suggest the presence of fewer lattice defects, which might lead to a decrease in the recombination of photogenerated charge carriers and thereby an increase in photocatalytic activity.

Several authors show the relationship between particle size and surface area (Parida et al., 2010). In general, smaller particles in a sample lead to a higher surface area, as reported in the literature (Parida et al., 2010; see **Table 3**). Also, nanomaterials' small size and large surface area are preferred to facilitate the charge transfer between the catalyst and the redox molecules, thus achieving a high catalyst activity (Hsieh et al., 2019).

4.1.2 Shape Effect on Band Gap

The band gap energy depends, in addition to the size, on the nanomaterials' shape, and this is based on the fact that the cohesive energy of nanostructured materials is different from that of bulky materials (Sapra and Sarma, 2004). The surface/volume ratio of nanomaterials plays an important role in characterizing their properties; therefore, it is essential to analyze them. The energy due to the contributions of the interior and surface atoms is defined as the cohesive energy, which we can express in relation to the energies for nano and bulky materials as follows:

TABLE 4 | N/n ratio for different nanosolids (Qi and Wang, 2004; Qi, 2005).

Nanosolid	*N/n*	Band gap energy (eV)
Nanosphere	$4d/D$	$E_g(D) = E_g(D_b)(1 - \frac{2d}{D})$
Nanotetrahedra	$4\sqrt{6}d/a$	$E_g(a) = E_g(D_b)(1 - \frac{2\sqrt{6}d}{a})$
Nanohexahedra	$4d/a$	$E_g(a) = E_g(D_b)(1 - \frac{2d}{a})$
Nanoctahedra	$2\sqrt{6}d/a$	$E_g(a) = E_g(D_b)(1 - \frac{\sqrt{6}d}{a})$
Nanodisk	$[1/h + 2/l]4d/3$	$E_g(l,h) = E_g(D_b)(1 - \frac{2d}{3}[\frac{1}{h} + \frac{2}{l}])$
Nanowire	$8d/3l$	$E_g(l) = E_g(D_b)(1 - \frac{4d}{3l})$
Nanofilm	$4d/3h$	$E_g(h) = E_g(D_b)(1 - \frac{2d}{3h})$

$$E_n = E_b\left(1 - \frac{N}{2n}\right), \tag{4}$$

where n is the total number of atoms in the nanomaterial, N is the number of atoms on the surface, and E_n and E_b are the cohesive energies per mole of the nano and bulky material, respectively. On the other hand, considering the linear relationship between the melting temperature T_m and the cohesive energy (Rose et al., 1981) in addition to the exponential relationship between electrical conductivity σ with activation energy and temperature (Palstra et al., 1990), we can arrive at the following equation:

$$\frac{E_a(D)}{E_a(D_b)} = \frac{T_{m,n}}{T_{m,b}}, \tag{5}$$

where $T_{m,n}$ and $T_{m,b}$ are the melting temperatures of the nano and bulky material; $E_a(D)$ is the activation energy,

TABLE 5 | Band gap values in accordance with the edge length of hexahedric metal halide perovskites.

Edge length (nm)	Band gap energy (eV)
12.9	1.56
11.5	1.59
9.9	1.63
8.1	1.66
7.6	1.72

material's size function, which is interpreted as $E_a(D) = E_c - E_F$, where E_c is the conduction band energy and E_F is the Fermi energy, and considering it as the middle of the band gap for most semiconductors, so the activation energy E_a becomes $E_a = E_g/2$, which leads to a change in the activation energy proportional to the band gap energy. Considering all of the above, the following equation is reached:

$$E_g(D) = E_g(D_b)\left(1 + \frac{N}{2n}\right), \tag{6}$$

where D and D_b are the size of the nano and bulky material and the value of $N/2n$ depends on the size and shape of the nano solid. N/n are the ratios for different systems that were reported (Qi and Wang, 2004; Qi, 2005; see **Table 4**).Here, N is the surface atom in different shapes, n are the total atoms in nano solids, d is the atomic diameter, D is the nanosphere diameter, a is the edge of each nano solid geometric, and l and h are the diameter and the height for the nanodisk considered for a specific case: $h \gg l$, where the nanodisk can be thought of as a nanowire, and when $l \gg h$, the nanodisk can be thought of as a nanofilm. Nanowire and nanofilm can be thought of as two disc-shaped nano solid boundaries.

The band gap of perovskites can be broadly tuned with a light emission that varies from the wavelength of ultraviolet (UV) to near infrared (NIR). Quingdong et al. (Ou et al., 2019) reported that this was due to dimensionality. In the case specific to hexahedric metal halide perovskites, due to quantum confinement, band gap energy increases in the counterpart of its bulky counterpart continuously by gradually reducing the size of $FaPbI_3$ perovskites (Li et al., 2018; see **Table 5**).

4.1.3 Effect of Defect on Band Gap

Particles formed after the synthesis process and thermal treatment contains surface defect owing to the reaction process. In this sense, it is essential to understand the nature and influence of surface chemical states on the photocatalytic activity of perovskites for further optimization of this photocatalytic system. Some analysis techniques such as X-ray photoelectron spectroscopy (XPS) allowed a quantitative and qualitative analysis of these defects and chemical states of the surface composition (Patil et al., 2021). This review will discuss the consequences of surface defects in the band gap and their consequence on photocatalytic activity, and the nature of these

TABLE 6 | Band gap in perovskites from DFT.

Name	Band gap (eV)	Reference
$BaTiO_3$	1.830	Jain et al. (2013)
$KNbO_3$	1.558	Jain et al. (2013)
$SrTiO_3$	1.827	Jain et al. (2013)
$CaTiO_3$	1.891	Jain et al. (2013)
$TiPbO_3$	1.760	Jain et al. (2013)
$ZrPbO_3$	3.248	Jain et al. (2013)
$FeBiO_3$	1.320	Jain et al. (2013)
$MgSiO_3$	5.454	Jain et al. (2013)
$FeSiO_3$	2.814	Jain et al. (2013)
$YAlO_3$	5.540	Jain et al. (2013)
$LuAlO_3$	5.743	Jain et al. (2013)

superficial states will not be analyzed. Under these circumstances, the nanostructured synthesis of perovskite structure has become an effective tool for diminishing surface states' contribution toward the optical properties because they have a large surface-to-volume ratio. Although the band gap variation is dependent on particle size, it also might be due to a surface effect (Oksenberg et al., 2020).

Defects are known to manifest themselves in the band structure of a material as an energy level within the band gap that depends on the properties of the defect. When the defect is created (product by the example of calcination or doping), such as oxygen vacancy from the crystal lattice of perovskite structure of $SrTiO_3$, $BaTiO_3$, $SrTiO_3$, and $SrSnO_3$, among others, two electrons are released into the conduction band as follows: $\frac{1}{2}O_{lattice} \rightarrow V_O^{2+} + \frac{1}{2}O_2 + 2e^-$, where $O_{lattice}$ is oxygen on a lattice site, V_O^{2+} are ionized oxygen vacancies in the perovskite structure, O_2 is oxygen in the atmosphere, and e^- are electrons. The oxygen vacancy is considered a donor with the defect state lying below the conduction band; thus, the difference between band conduction and the defect level is equal to the defect ionization energy. In addition, the released oxygen leaves vacancies behind, which promotes diffusion through the solid and reduces the band gap. The effect of particle size contributes to changing the density of defects and can lead to slightly different band gaps. Chen et al. (2017) demonstrated that the high-pressure hydrogenation process influences the formation of surface vacancies in the $BiFeO_3$ nanoparticles, which was corroborated by XPS spectroscopy. With increasing hydrogenation temperature, the oxygen vacancy concentration increased. The formation of surface oxygen vacancies contributes to the following: 1) narrow $BiFeO_3$ band gap, leading to an enhanced light absorption capability, 2) suppressing the recombination of photogenerated electrons and holes, 3) facilitating the photoinduced charge separation and transfer process, and 4) enhancing the adsorption capability for the methyl orange molecules, leading to a high photodegradation. Therefore, the high-pressure hydrogenation process in $BiFeO_3$ contributed to the enhanced photocatalytic activity.

Theoretical study using first principles showed that the substitution of 3D cations induces an occupied energy level either in band valence or in band gap on account of the t_{2g} level of substituent (Fang et al., 2019; Zhu et al., 2019). Fang et al. (2019) showed that the substitution of metal cation in the

TABLE 7 | Band gap values following the substitution in the A-site, B-site, and X-site in halide perovskites.

A-site	Band gap (eV)	B-site	Band gap (eV)	X-site	Band gap (eV)
[a]$CsGeI_3$	1.6	[b]$MAPbCl_3$	2.9	[b]$CsPbCl_3$	2.7
[a]$MAGeI_3$	1.9	[c]$MASnCl_3$	2.8	[b]$CsPbBr_3$	2.4
[a]$FAGeI_3$	2.2	[d]$MAGeCl_3$	3.7	[b]$CsPbI_3$	1.8
[b]$CsPbI_3$	1.8	[b]$FAPbI_3$	1.4	[d]$CsSnCl_3$	2.8
[b]$MAPbI_3$	1.5	[c]$FASnI_3$	1.4	[d]$CsSnBr_3$	1.8
[b]$FAPbI_3$	1.4	[d]$FAGeI_3$	2.2	[c]$CsSnI_3$	1.3

[a]*Saparov and Mitzi (2016).*
[b]*Wu et al. (2018).*
[c]*Toshniwal and Kheraj (2017).*
[d]*Hoefler et al. (2017).*

$Bi_xSr_{1-x}TiO_3$ structure gives rise to energy levels that appeared within the forbidden band and caused a narrowing of the band gap. The Materials Project initiative (Jain et al., 2013) presents a compilation of band gap energies from different perovskite materials from DFT results (see **Table 6**). Other parameters, that is, variation in crystallite size, structural deformation, and surface area/volume ratio, might have a specific effect on the optical energy band gap. Although many methods, such as modulating band gap, employment of composite semiconductors, metallic or non-metallic doping, regulating nanoscale morphology and structure, and introducing defects in the lattice, have been utilized to enhance the photocatalytic activity, effective carrier separation is still far from improving its photocatalytic efficiency.

4.1.4 Effect of Doping on Band Gap

Another parameter to band gap modulation is doping. The implication of the doping, with cations of different sizes, for band gaps was observed in the different perovskite types. Several studies showed a significant band gap tuning in doped-perovskite oxide as a function of the dopant element and the synthesis process. To $LaNiO_3$ doped with ions of Gd, Fe, and Co with different ratios, a significant decline in the Eg values from 2.90 to 2.43 eV was shown. The band gap decrease might be due to the deformation induced in Fe–O octahedral or rearranging of the molecular orbitals (Ghafoor et al., 2021). However, the substitution generates certain impurities within the forbidden band, which facilitates the narrowing of the band gap. Yang et al. (2019) calculated the E_g for $BiFeO_3$ and $BiFeO_3$:Gd^{3+} being 2.28 and 2.17 eV, respectively. Such results indicate that $BiFeO_3$:Gd^{3+} is an excellent photocatalyst and has potential applications in photocatalytic hydrogen production. They indicate that the doping Gd^{3+} induces the formation levels in the forbidden band, leading to a decrease in Eg; however, increased oxygen vacancies also exist, which could contribute to the decrease of E_g. On the other hand, it is clear that the doping is escorted by the generation of defects that are likely to behave as recombination centers of $e^- - h^+$, leading to charge carrier transferring to the interface or surface being more difficult. Thus, if the density of defects is high, photoactivity cannot be enhanced. The control of the density of defects in doped perovskites is essential and plays a key role in enhancing photocatalytic performance.

In halide perovskites, different physical properties can be modified by substitution in the A-site, B-site, or X-site. The A-site substitution can improve the overall stability by tuning the tolerance factor. B-site substitution can reduce the harmful Pb content and improve phase stability by altering the B–X bond length. X-site substitution can tune the band gap by changing the ratio of mixed-halide ions (Lu et al., 2020). The variation in the band gaps in halide perovskites changes with cell volume (Borriello et al., 2008), as follows: $\alpha_V = (\partial E_g/\partial lnV)$, where α_V is 2.45 eV to $MAPbI_3$. In accordance to **Table 7**, we can observe that the substitution in A-, B-, and X-site will get to modulate the band gap. The importance in choosing the composition in halide perovskites lies in the optimization of the photocatalytic properties and stability. The band gap changes on halide perovskite substitution are influenced more by the electronic states of the anion, that is, from Cl to Br to I, the valence band composition changes from 3p to 4p to 5p with a monotonic decrease in electron binding energy (lower ionization potential). The substitution of Cl by I or Br by I in $CsPbX_3$ has been shown to decrease the band gap from 2.7 to 1.8 eV and 2.4 to 1.8 eV, respectively (see **Table 7**). Thus, the shift of E_g values to low energy, visible-light absorption enhanced significantly and, consequently, the photocatalytic activity.

4.2 Lifetime of the Charge Carriers in Perovskites

For a photocatalyst, beyond the surface area, chemical defect, and band gap, the effective generation, separation, and recombination of $e^- - h^+$ pairs influence photocatalytic activity. The charge-carrier lifetime in general describes the dependence of the electron or hole concentration as a function of time after the generation of electrons and holes (Krückemeier et al., 2021). Nevertheless, the lifetime of charger carriers in perovskite structure still has data shortage and requires a quantitative study (Serpone et al., 1995). Sheng et al. (2020) claimed that a longer lifetime can facilitate the photoexcited charge carriers to reach the active sites to complete the surface redox reactions. Thus, perovskite materials with prolonged lifetime enhanced charge separation and favor the slow kinetics of pollutant degradation, mainly attributed to the difficulty in reacting the aliphatic group with organic OH-terminated surfaces. Also, it is necessary to indicate that ligand modifications in pollutants affect the lifetimes of the photocatalysts. Tang et al. reported that the lifetime of the trapped charge carriers depends on the excitation energy (Tang et al., 2008).

Analysis of $BiFeO_3$:Gd^{3+} nanoparticles from photocurrent curves and electrochemical impedance spectra show a higher photocurrent intensity than $BiFeO_3$, which suggests the higher efficient generation and separation of $e^- - h^+$ pairs and the longer lifetime of charger carriers for $BiFeO_3$:Gd^{3+} (Yang et al., 2019). The ion Gd^{3+} benefits the separation of $e^- - h^+$ pairs and promotes the charger transfer to the surface. This prolonged lifetime improves redox reactions, thus optimizing photocatalytic activities. Similar behavior was observed in $CaTiO_3$ when treated at 0.1 M $NaBH_4$ solution when

compared to $CaTiO_3$ (Yan et al., 2018). The result reveals that 0.1 M-$CaTiO_3$ exhibits an enhanced photocurrent density compared to $CaTiO_3$ and, likewise, a longer lifetime of charger carriers. In this case, the $NaBH_4$ solution formed a disordered layer and, simultaneously, disordered surface states are introduced in the forbidden gap of $CaTiO_3$. Furthermore, the disordered surface states can act as electron acceptors and trap photogenerated electrons, and this contributes to suppressed $e^- - h^+$ recombination and promotes the increase of photogenerated h^+ that are fundamental in photocatalytic reactions. The charge carrier lifetimes can be affected by particle size, as suggested by Sieland et al. (2018). Small particles exhibit longer charge carrier lifetimes and higher photonic efficiencies, while large particles increase the charge carrier recombination and decrease the lifetimes. Such results are according to theoretical study (Liu and Zhao, 2010).

In halide perovskites, the lifetime was determined by employing time-resolved photoluminescence spectroscopy. The result indicates that the substitution in the X-site decreases the lifetime values of 4.38, 0.73, and 0.86 ns for $Cs_2AgBiCl_6$, $Cs_2AgBi(Br_{0.5}I_{0.5})_6$, and Cs_2AgBiI_6 nanocrystals, respectively (Wu et al., 2021). Much longer lifetimes have been found in $Cs_2AgBiBr_6$, around 660 ns (Slavney et al., 2016). The longer lifetime helps charge carriers in motion to reach active sites on the surface, consequently promoting the surface redox reactions. On the other hand, perovskite heterojunctions are emerging as a promising material for high-performance photocatalytic applications. The heterojunctions present two independent band gaps, which overlapped, and hence, $e^- - h^+$ can be shuttled in direct migration from one level to another through the interface (Schottky barrier) (Guleria et al., 2021). The Schottky barrier is that through which $e^- - h^+$ movement inhibited the charge carrier recombination and thus prolonged the lifetime of $e^- - h^+$ pairs. This strategy applied to pure or doped perovskites is promising and will significantly improve the photoactivity for water treatment. For example, Ravi et al. (2020) showed that in nanocrystalline halide perovskite $CsPbBr_3$/ZnS (core/shell), the average lifetime is 102.6 ns, which is about 15 times longer than the average lifetime (7.2 ns) of nanocrystalline $CsPbBr_3$. These results confirm that our ZnS shell growth effectively modifies the electronic properties of the core. In addition, band edge alignment at the core/shell interface can explain the significantly longer lifetime. Also, the slow decay $CsPbBr_3$/ZnS when compared to CsPbBr3 demonstrates that $CsPbBr_3$/ZnS increases the lifetime of the charge carriers and may improve photocatalytic performance. Kirchartz et al. (2020) suggested that the lifetime depends on defect concentrations.

The importance of the lifetime of the charge carriers lies in the possibility of determining the efficiency of the photocatalytic performance, as longer-lived carriers will have a higher probability of reaching the interface, that is, recombination will be limited (or will not lead to recombination losses) by the time the electrons take to diffuse through the perovskite layer. Thus, in an efficient photocatalytic process, the charge carriers combine radiatively, and techniques such as time-resolved photoluminescence spectroscopy become a powerful tool to monitor the charge carrier lifetime and further the understanding of the perovskite photocatalytic process.

4.3 Band Edges Relative to the Redox Potential of Water Splitting

The band gap of the perovskite structures is essential for improving light absorption and charge carrier generation and depend on valence band and conduction band positions. These characteristics lead to high performance for CO_2 reduction, N_2 reduction, and water splitting. However, another important parameter is the position of valence- and conduction-band edges relative to the water redox potential levels, which are also critical factors governing photocatalytic water splitting activity, where the band edges should be close to the required redox potentials to enable the photocatalytic process. Such parameters will determine the hydrogen and oxygen evolution reactions under light. Thus, in the process of water splitting the charge transfer between the interface and optical transitions are depending strongly on the nature of the band edge. Hydrogen evolution reactions (HERs) occur when the conduction-band edges are more negative than the hydrogen evolution potential level, H^+/H_2. Oxygen evolution reactions (OERs) occur when the valence-band edges are more positive than the oxygen evolution potential level, H_2O/O_2. A representation is shown in **Figure 8**.

Although an appropriate band gap of 1.23 eV is necessary for the potential for the water splitting process, and its band edges do not straddle the HER and OERs. The band edge positions relative to the water redox potential levels are significantly influenced by the material, crystal structure, surface characteristics, and operating environment of a photocatalyst (Park and Kolpak, 2019). In perovskite structure $MLnTa_2O_7$ (M = Cs, Rb, Na, and H; Ln = La, Pr, Nd, and Sm), the photocatalytic activity is sensitive to Ln and M. The highest activity was obtained for Ln = Nd, where the activity decreased in the sequence of Rb > Cs > Na > H (Machida et al., 2003). The band gap energy is strongly dependent on Ln, but negligibly affected by M. The effect of Ln can be explained by the shift of the Ln 4f levels from the conduction-band edge to the valence-band edge with increasing numbers of Ln 4f electrons, suggesting that lanthanide 4f shell affects the positions of not only the valence-band edge but also the conduction-band edge and played an important role in photocatalytic reaction. The band edge alignments relative to the water redox potential levels at the interface directly influence light absorption, the energies of photogenerated charge carriers, and photocatalytic reactions at the surfaces. Burnside et al. (1999) argued that the nanometer-sized $SrTiO_3$ particles induced a quantum confinement effect and resulted in changes in the band structure. The nanosheets had a 0.16-eV wider band gap and a 0.47-eV raised CB edge, as compared to a commercial WO_3. Xie et al., on the other hand, assumed that the band structure of WO_3 can be engineered by exploiting the crystal facet–dependent electronic structure effect.

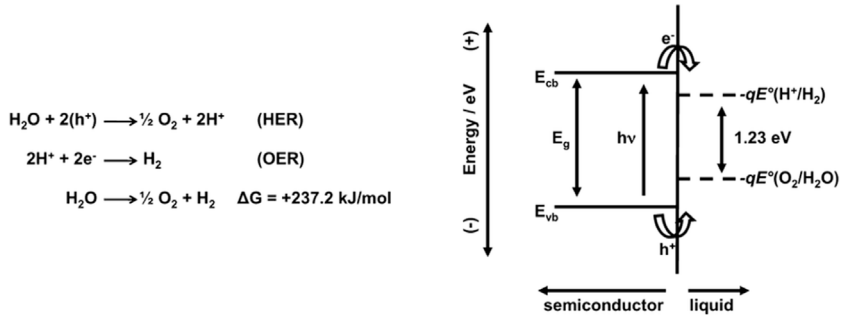

FIGURE 8 | Oxygen evolution reaction (HER) and hydrogen evolution reaction (OER) for overall water splitting (under acidic conditions); ideal semiconductor material for splitting water at its surface under illumination with absolute energy scale represented [left vertical axis (–) and (+)] for E_{cb} and E_{vb} and the electrochemical potentials given by –qE°, where E° is the reduction potential for both (H^+/H_2) and (O_2/H_2O) redox couples (Walter et al., 2010).

The authors showed that WO_3 nanosheets with exposed {002} crystal facets reduced CO_2 to CH_4, whereas WO_3 cubes with equal amounts of {200}, {020}, and {002} facets were inactive. The authors proposed that {002} crystal facets have a higher CB edge than the bulk WO_3 due to the different atomic structures.

In halide perovskite $CsPbX_3$ (X = Cl, Br, I) the modification of site-X significantly contributes to the valence-band edge with excitonic transition probability decreasing from X = Cl to Br to I, without changing the size of the nanocrystals (Ravi et al., 2016; Ravi et al., 2020). When compared, ZnS and $CsPbBr_3$ both have similar valence-band edges, while the conduction-band edge of ZnS > that of $CsPbBr_3$. However, the formation of $CsPbBr_3$/ZnS (core/shell) nanocrystals enables the alignment at the core/shell interface where the hole is delocalized over both the core and shell and the electron is localized inside the core. In order to optimize the determination of band edge, studies using first-principles density functional theory calculations help to predict the environment-dependent band edge positions in vacuum and water (Park and Kolpak, 2019).

Some successful strategies of band structure include modification of the surface composition, quantum confinement, crystal facet–dependent electronic effect, and chemical modification. On the other hand, light-harvesting can be improved by modification with either organic or inorganic components: metal oxides and sulfides, carbon allotropes, dyes and other optically active molecules, and plasmonic nanoparticles. However, the inclusion of new strategies also gives rise to common problems, such as quenching of photoluminescence, multiple nanocrystalline cores inside a single shell, and an insulating shell that prevents the charge transport. Thus, an ideal photocatalyst to the CO_2 conversion should possess 1) possibly a large surface area with favorable chemistry and energetics, 2) well-developed suitable porosity with good mass transfer properties, 3) a narrow band gap and good light-harvesting properties, 4) valence-band and conduction-band edges positioned properly to drive both CO_2 reduction and H_2O oxidation, 5) high purity and crystallinity, 6) proper morphology with a short bulk-to-surface distance, and 7) an efficient spatial charge separation (Marszewski et al., 2015).

Different physical and chemical parameters must be considered in perovskite material to make them photocatalyzed with high performance. Among them, the contributions of band gap, lifetime of the charge carriers, and band edges relative to the redox potential in perovskites play a vital role in photocatalytic activity. In this sense, different strategies were adopted to maximize the performance of the photocatalysts. As previously shown, particle size, doping, and chemical defect influence the band gap and lifetime of the charge carriers. Other factors are associated as shape, composition, substitution in the A-site, B-site, or X-site facility, and the light absorption owing to the narrowing of E_g; this has the objective of taking advantage of the dominant solar irradiation. In addition, fabricate photocatalytic material with a longer lifetime of charger carriers to suppress the process of $e^- - h^+$ recombination and prolong the lifetime of $e^- - h^+$ pairs.

5 APPLICATIONS OF HALIDE AND OXIDE PEROVSKITES TO WATER TREATMENT

Owing to its unique optical properties and versatility in halide and oxide perovskites, these materials become a compelling platform well suited to emerging applications. In this section, some photocatalysis-based applications of halide and oxide perovskites, including water splitting, photocatalytic CO_2 reduction, and photocatalytic N_2 reduction, are discussed briefly, in order to motivate new applications in water treatment.

5.1 Perovskite Materials to Water Splitting

Perovskite-based compounds are photoactive materials that have been widely investigated for photocatalytic water splitting (Wang et al., 2017b). This process originates from the conversion from the absorption of sunlight to produce an electron-hole pair for photocatalytic water splitting in oxygen and hydrogen, that is, water molecules are oxidized by the holes to protons and O_2, and the released protons are reduced by the electrons to H_2. The chemical reaction is $2H_2O \rightarrow 2H_2 + O_2$. However, due to the loss of the charges through e^--h^+ recombination processes, which decreases the number of electron–hole pairs *via* proton

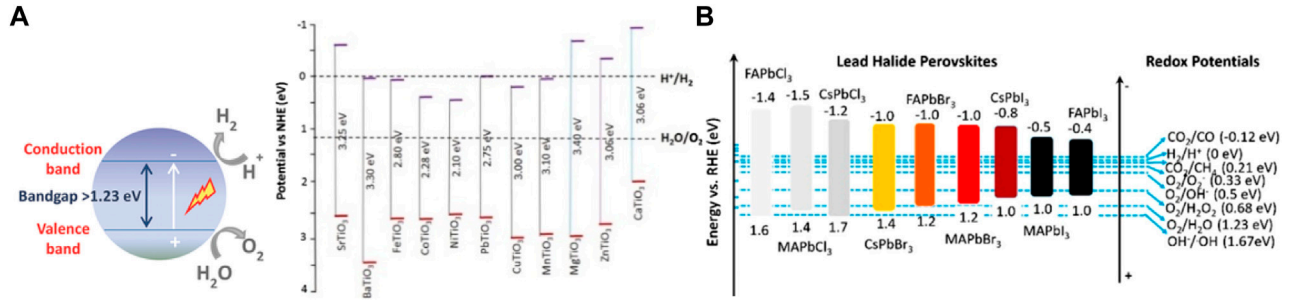

FIGURE 9 | Band gaps and band edges with respect to the redox potential in **(A)** schematic of water splitting using photocatalyst of oxide perovskites (Bin Adnan et al., 2018) and **(B)** halide perovskites (Romani and Malavasi, 2020).

regeneration or light emission; the water-splitting efficiencies reported so far are limited. Other, no less important, factors making the high-efficiency photocatalytic materials difficult include inferior durability, slow kinetics, poor sunlight absorption, and poor charge carrier separation capability of photocatalysts. In addition, theoretical studies show that the energetic reaction required for the separation of water into H_2 and O_2 corresponds to 1.23 eV (1,100 nm) (Wang et al., 2017b). However, some perovskites (halide and oxides) do not have suitable band structures that are favorable, that is, 1.23 eV, impeding their use as highly efficient photocatalysts. Likewise, the lower level the conduction band should be more negative than the redox potential of H^+/H_2 (0.0 V vs. normal hydrogen electrode (NHE) at pH = 0), while the level tops the valence band should be more positive than the redox potential of O_2/H_2O (1.23 V vs. NHE at pH = 0) (Maeda and Domen, 2007). Halide and oxides perovskites the band gaps and band edges with respect to the redox potential is shown in **Figures 9A,B**. Among other advantages, perovskites offer flexibility in the composition, either in site A or B, which allows you to adjust the band structure, as mentioned in the previous section. The latter allows optimizing the water splitting and its functionalities.

Oxide-based perovskite materials are photoactive materials, and the structure type $ATiO_3$ (A = Ba, Sr, Ca, Mg, and Mn) has been reported as stable and suitable materials as water splitting, due to its functionality, and is likely to be the most cost-effective approach to achieve water splitting (Osterloh, 2008; Kudo and Miseki, 2009). Oxide perovskites reveal several advantages such as enhanced charge separation, excellent thermal stability, high chemical stability, large optical absorption coefficients, and extended electronic carrier diffusion lengths. The majority of oxide perovskite band gaps are above 3 eV and do not meet the criteria for photocatalytic water splitting. However, there are some oxide perovskites that have a narrow band gap such as $LaFeO_3$, $BiFeO_3$, and $BaTiO_3$ (Parida et al., 2010; Yang et al., 2019; Clabel H. et al., 2021a). When oxide perovskites are doped, their structure can be tuned and holds great promise for water splitting. In doped perovskites, the band gap of the compound material is decreased and it apparently becomes a UV-visible-light response photocatalyst. In order to maximize the functionality of water splitting, the perovskite structure was doped, and the most common materials for water splitting under UV and visible-light are Mn-, Ta-, and Nb-based perovskite oxides. Yang et al. studied the effects of Sr-doped $LaMnO_3$ perovskites, targeted for thermochemical dissociation of water splitting (Yang et al., 2014). Studies for visible light photocatalytic hydrogen production from water splitting in pristine and chalcogen-doped $BaTiO_3$ were realized by first-principles DFT (Huang et al., 2019). The doped chalcogens can significantly decrease the band gap of $BaTiO_3$, and this is especially true for the larger concentration of the dopant, leading to significant reduction from 3.13 to 1.01 eV, satisfying the conditions of water splitting. Luo et al. studied the effect of B and Fe co-doping $SrTiO_3$ in the band gap (Humayun et al., 2018). The co-doping leads to the band gap of $SrTiO_3$ being significantly reduced from 3.4 to 1.9 eV. The band gap of B and Fe co-doping $SrTiO_3$ is significantly reduced and exhibits absorption up to a wavelength of 650 nm. This confirmed the enhanced charge carrier separation and improved photocatalytic activities of the photocatalysts for CO_2 conversion and water splitting.

Also, halide perovskites are used as an efficient compound for water splitting. Mainly, halide perovskite $CH_3NH_3PbI_3$ exhibits clear ambipolar nature of charge carrier transport, a behavior where both electrons and holes exhibit very good mobility. Because of this unique property, $CH_3NH_3PbI_3$ can be used as both photoanode for water oxidation and photocathode for water reduction reaction (Singh et al., 2020). However, due to Pb^{2+} toxicity, B-sites in the perovskite structure have been explored. Also, in another work, using lead-free and phase-stable Sn(II) halide perovskite $CH_3NH_3SnI_3$ has been prepared and tested (Yang et al., 2015; Volonakis and Giustino, 2018). This Sn(II) perovskite has a band gap of 1.3 eV, with charge carrier mobility of $\approx 1.6\ cm^2\ V^{-1}\ s^{-1}$, and demonstrated photocatalytic H_2 evolution making them functional for water splitting. Other alternatives of potentially promising materials of lead-free halide perovskites are $Cs_2BiAgCl_6$, $Cs_2BiAgBr_6$, $Cs_2SbAgCl_6$, and $Cs_2InAgCl_6$ (Volonakis and Giustino, 2018). The electronic properties and ionization potential were studied from first principles examining the different possible surface terminations and the thermodynamic stability. It was found that the band levels of $Cs_2BiAgCl_6$ and $Cs_2BiAgBr_6$ are matching the redox potential of water. $Cs_2SbAgCl_6$ and $Cs_2InAgCl_6$ could also be suitable for hydrogen evolution or water evolution, and such factors are favorable to water splitting.

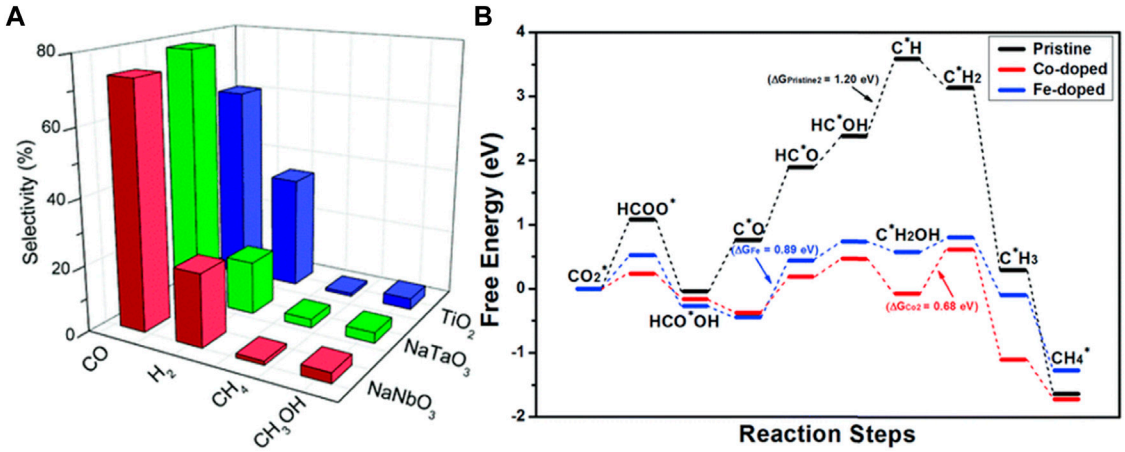

FIGURE 10 | (A) Selectivities toward the main products obtained in the photocatalytic reduction of CO_2 over $NaNbO_3$, $NaTaO_3$, and TiO_2, **(B)** The free energy diagrams of the most favored paths of CO_2 reduction on pristine, Co-doped, and Fe-doped $CsPbBr_3$ perovskite cases (Fresno et al., 2017; Tang et al., 2019).

5.2 Perovskite Materials to Photocatalytic CO_2 Reduction

As a result of human activity and industrial development, concentrations of carbon dioxide have increased in recent decades. In this scenario, a possible way is the use of highly active photocatalytic systems for photocatalytic reduction of CO_2, leading to hydrocarbons in the gas phase and oxygenates in the liquid phase (Hong et al., 2013), with the aid of solar energy. Several mechanisms are crucial for improving the photoactivity: 1) surface area, 2) surface energetics, 3) mass transfer phenomena, 4) light absorption, 5) excitation (bulk and surface recombination), and 6) charge separation (Marszewski et al., 2015). These important aspects will impact the performance of a photocatalyst. The CO_2 adsorption by physisorption and chemisorption, where the molecule is susceptible to reduction by photogenerated electrons, these electrons are generated through light absorption, excitation, and charge separation. The CO_2 adsorption is promoted by several factors physical and chemical as the increase of catalyst surface area, surface defects, basic sites, and Cu and/or Pt co-catalyst nanoparticles surfaces. Oxide and halide perovskites due to their high reactivity surface and tuning of physical and chemical properties can lead to a significant improvement of photoelectrochemical activities (Shi and Zou, 2012; Xu et al., 2017).

Perovskite oxide type $NaNbO_3$ and $NaTaO_3$ prepared by solid-state reactions were applied for the photocatalytic reduction of CO_2 (Fresno et al., 2017). Due to extrinsic and intrinsic properties, such as surface area, structural modification, e^--h^+ recombination, and the reducing potential of conduction band electrons, a competition of water protons for photogenerated electrons leads to greater performance in CO_2 reduction. The main products obtained in the photocatalytic reduction of CO_2 over $NaNbO_3$ and $NaTaO_3$ is shown in **Figure 10A**. Hemminger reported the role of $SrTiO_3$ perovskites for photocatalytic reduction of CO_2 to CH_4 production (Hemminger et al., 1978). Co-catalysts nanostructured perovskite oxides also exhibit a band edge tuning, long charge diffusion lengths, longer charge carrier lifetimes (not in all perovskite oxides), and structural good stability (Shi et al., 2017). Au/Rh nanoparticle addition in $SrTiO_3$ showed good photocatalytic performance for CO_2 reduction and water splitting in the visible light spectra, and the degree concentration of the Au/Rh ratio leads to variation in the CO_2 reduction (Li et al., 2016). The difference in the transfer of interband-transition photoelectron from $SrTiO_3$ to Rh and Rh/Au@$SrTiO_3$ was evidenced by photoluminescence spectra, in this last in low photoluminescence evidence that recombination between the photoelectron and the positive-charged Au is suppressed. In addition, Rh as co-catalyst has a function as accumulated photoelectrons. Thus, the photoelectrons induced by interband transition and plasmon resonance in Au indeed transfer from $SrTiO_3$ to the Rh co-catalyst during visible light irradiation, leading to both suppressing the CH_4 production and significantly enhancing the photoactivity. The improved performance of photocatalytic reaction can also be enhanced by other transition metal co-catalysts which extend visible light absorption through localized surface plasmon resonance of metal nanostructures, such as Ag, Pt, Ir, and Cu (Wood et al., 2001; Kamat, 2012). In addition, the interface between the metal and semiconductor type perovskite, a Schottky barrier, is formed, where the work function difference gives rise to a potential offset. Such Schottky barriers can reduce the kinetics of electron flux from the perovskite conduction band into the metal, that is, transfer of photogenerated electrons across the interface. This accumulation of photogenerated electrons on the metal enhanced the performance in the CO_2 reduction (Wood et al., 2001).

Light-emitting lead halide perovskite nanocrystals $CsPbBr_3$ were explored for catalytic CO_2 reduction (Shyamal et al., 2020). Shyamal et al. (2020) showed the surface facet-dependent catalytic activities in cube and faceted non-cube shapes, where the adsorption/desorption and the suppression of carrier recombination are essential in the CO_2 reduction. Surfaced isotropic polyhedron-shaped poor emitter noncubes were observed to be the superior catalyst. Moreover, the DFT study will reveal that the adsorption/desorption of CO_2 and reduction have an efficient activity along with the {112} and {102} facets compared to the dominant {110} and {002} facets of orthorhombic cube-shaped $CsPbBr_3$ nanostructures. A size-dependent enhancement

in photocatalytic degradation has been previously established for Au-TiO2 composites. Using density functional theory (DFT), the enhancement of the photocatalytic capability was shown in pristine $CsPbBr_3$ perovskites and doped $CsPbBr_3$ perovskites, which transform CO_2 into methane (Tang et al., 2019). Doped $CsPbBr_3$ with Co, Fe, Ni, Cu, Ag, Mg, Mn, and Bi shows a better catalytic performance than pristine $CsPbBr_3$. Particularly, Co- and Fe-doped $CsPbBr_3$ perovskites are promising candidates due to the better adsorption, promoting the CO_2 reduction process. The CO_2 reduction process is mainly reduced to HCOO* in the hydrogenation, through successive proton absorptions on the O and C atom generating C*H and C*H_2 for the pristine and Co- and Fe-doped $CsPbBr_3$ perovskites, respectively, releasing H_2O and then hydrogenating to CH_4 (see **Figure 10B**). The free energy barrier is 1.20, 0.68, and 0.23 eV for the pristine, Co-doped, and Fe-doped $CsPbBr_3$ perovskites, respectively, thus showing the catalytic efficiency in Co and Fe doped $CsPbBr_3$ perovskites. Such results are consistent with the previous experiment (Xu et al., 2017).

6 CONCLUSION AND OUTLOOK

Investigations into the use of photocatalytic perovskites for the elimination of emerging contaminants are of great current interest. A suitable band gap taking advantage of dominant solar irradiation and high photoinduced charge separation efficiency are key factors for ideal photocatalysts and are under constant research. A wide range of synthesis methods allows the creation of unique structures that can enhance photocatalytic activity, as evidenced by the other research group in this area. The present review focuses on three parameters essential in photocatalytic activity: the role of band gap, band edges, and the lifetime of charger carriers. Additionally, the electronic properties as the band gap can be affected in many different ways for all types of perovskite structures. In pure perovskites and doped perovskites with single-phase structures, factors of calcination temperature, doping, the concentration of doping, composition, and density of defect can affect the band gap. Synthesis methods also determine the band gap characteristics where the shape and size drive the formation of different facets, surface area, and porosity. Different mechanisms for reducing the band gap (<3 eV) in order to improve the narrow light-response to the ultraviolet spectrum (~4% of sunlight) and inhibit the recombination process were considered, thus improving photocatalytic efficiency. The fundamental understanding of such mechanisms helps provide much broad insight into the role of band gap and lifetime in advanced perovskites applied to photocatalysis. An attempt is realized in this review to differentiate the contribution between both band gap and lifetime of charger carriers.

The narrow band gap is mainly considered to play an important role in light absorption capability, though the modulation of band gap is dependent on both extrinsic and intrinsic parameters. Changes in the defect density at the surface can impact the redox reaction at the surface and band gap. The particle size influences the band gap due to the confinement of the electrons; likewise, the small size and large surface area of nanomaterials are preferred to facilitate the charge transfer between the catalyst and the redox molecules. Doping has been shown to alter the optical properties of perovskite structures and improve their stability. Meanwhile, the lifetime of charger carriers is considered necessary because it facilitates the photoexcited charge carriers to reach the active sites to complete the surface redox reactions. In addition, it promotes the increase in photogenerated $e^- - h^+$ that are fundamental in the photocatalytic reactions and suppresses the process of $e^- - h^+$ recombination. Moreover, the parameters of the band edges relative to the redox potential will determine the hydrogen and oxygen evolution reactions under sunlight, essential to water splitting performance.

Although the mechanisms of doping are effective in optimization, they merit a more thorough investigation. In this sense, a challenge is using the doping type within the host matrix, optimized substitution in the A-, B-, or X-site, and doping concentration. The complementation with current techniques that help identify and clarify the reaction mechanisms between the dopant and the matrix will contribute enormously to this challenge. Quantifying the defect density and identifying the type of defects present on the surface would help understand and interpret perovskite structures lifetime and decay kinetics. Although techniques such as transient absorption, time-resolved photoluminescence, and confocal microscopy explore the lifetime and energy transfer process in perovskite structures, these techniques only contribute to certain types of perovskites. Incorporating knowledge focused on surface science would be helpful in understanding the sites active in the surface affect redox reaction and at what level according to the type of defect. Additionally, theoretical calculations are also useful in helping to predict the observed effects, from the surface chemical defect, particle size, surface area, and porosity. Finally, the different types of perovskite structures are promising; however, we still have a broad horizon to explore to make it more efficient.

AUTHOR CONTRIBUTIONS

JH: conceptualization, methodology, investigation, visualization, and writing—original draft. JC-R: review investigation and writing. EJ: conceptualization, review and editing, and supervision.

FUNDING

This research was supported by the São Paulo Research Foundation (FAPESP) through the Centro de Pesquisas em Óptica e Fotônica (CePOF) under the grant 2013/07276-1 and Conselho Nacional de Desenvolvimento Científico e Tecnológico (CNPq) grant 310925/2017-7.

ACKNOWLEDGMENTS

This research was supported by the São Paulo Research Foundation (FAPESP) through the Centro de Pesquisas em Óptica e Fotônica (CePOF) under the grant 2013/07276-1 and Conselho Nacional de Desenvolvimento Científico e Tecnológico (CNPq) grant 310925/2017-7.

REFERENCES

Akkerman, Q. A., D'Innocenzo, V., Accornero, S., Scarpellini, A., Petrozza, A., Prato, M., et al. (2015). Tuning the Optical Properties of Cesium lead Halide Perovskite Nanocrystals by Anion Exchange Reactions. *J. Am. Chem. Soc.* 137, 10276–10281. doi:10.1021/jacs.5b05602

Alammar, T., Hamm, I., Grasmik, V., Wark, M., and Mudring, A.-V. (2017). Microwave-Assisted Synthesis of Perovskite $SrSnO_3$ Nanocrystals in Ionic Liquids for Photocatalytic Applications. *Inorg. Chem.* 56, 6920–6932. doi:10.1021/acs.inorgchem.7b00279

Bartel, C. J., Sutton, C., Goldsmith, B. R., Ouyang, R., Musgrave, C. B., Ghiringhelli, L. M., et al. (2019). New Tolerance Factor to Predict the Stability of Perovskite Oxides and Halides. *Sci. Adv.* 5, 1–10. doi:10.1126/sciadv.aav0693

Belver, C., Bedia, J., Gómez-Avilés, A., Peñas-Garzón, M., and Rodriguez, J. J. (2019). *Semiconductor Photocatalysis for Water Purification*, 581–651. doi:10.1016/B978-0-12-813926-4.00028-8

Bin Adnan, M. A., Arifin, K., Minggu, L. J., and Kassim, M. B. (2018). Titanate-Based Perovskites for Photochemical and Photoelectrochemical Water Splitting Applications: A Review. *Int. J. Hydrogen Energ.* 43, 23209–23220. doi:10.1016/j.ijhydene.2018.10.173

Borriello, I., Cantele, G., and Ninno, D. (2008). Ab Initioinvestigation of Hybrid Organic-Inorganic Perovskites Based on Tin Halides. *Phys. Rev. B* 77, 1–9. doi:10.1103/PhysRevB.77.235214

Brutchey, R. L., and Morse, D. E. (2006). Template-Free, Low-Temperature Synthesis of Crystalline Barium Titanate Nanoparticles under Bio-Inspired Conditions. *Angew. Chem. Int. Ed.* 45, 6564–6566. doi:10.1002/anie.200602571

Burnside, S., Moser, J.-E., Brooks, K., Grätzel, M., and Cahen, D. (1999). Nanocrystalline Mesoporous Strontium Titanate as Photoelectrode Material for Photosensitized Solar Devices: Increasing Photovoltage Through Flatband Potential Engineering. *J. Phys. Chem. B* 103, 9328–9332. doi:10.1021/jp9913867

Caruntu, D., Rostamzadeh, T., Costanzo, T., Salemizadeh Parizi, S., and Caruntu, G. (2015). Solvothermal Synthesis and Controlled Self-Assembly of Monodisperse Titanium-Based Perovskite Colloidal Nanocrystals. *Nanoscale* 7, 12955–12969. doi:10.1039/c5nr00737b

Chang Chien, S.-W., Ng, D.-Q., Kumar, D., Lam, S.-M., and Jaffari, Z. H. (2022). Investigating the Effects of Various Synthesis Routes on Morphological, Optical, Photoelectrochemical and Photocatalytic Properties of Single-Phase Perovskite BiFeO3. *J. Phys. Chem. Sol.* 160, 110342. doi:10.1016/j.jpcs.2021.110342

Chen, D., Cheng, Y., Zhou, N., Chen, P., Wang, Y., Li, K., et al. (2020). Photocatalytic Degradation of Organic Pollutants Using TiO_2-Based Photocatalysts: A Review. *J. Clean. Prod.* 268, 121725. doi:10.1016/j.jclepro.2020.121725

Chen, D., Niu, F., Qin, L., Wang, S., Zhang, N., and Huang, Y. (2017). Defective $BiFeO_3$ with Surface Oxygen Vacancies: Facile Synthesis and Mechanism Insight into Photocatalytic Performance. *Solar Energ. Mater. Solar Cell* 171, 24–32. doi:10.1016/j.solmat.2017.06.021

Chen, D., and Ye, J. (2007). $SrSnO_3$ Nanostructures: Synthesis, Characterization, and Photocatalytic Properties. *Chem. Mater.* 19, 4585–4591. doi:10.1021/cm071321d

Chen, P., Ong, W. J., Shi, Z., Zhao, X., and Li, N. (2020). Pb-Based Halide Perovskites: Recent Advances in Photo(electro)catalytic Applications and Looking Beyond. *Adv. Funct. Mater.* 30, 1–27. doi:10.1002/adfm.201909667

Cheng, C., Gao, S., Zhu, J., Wang, G., Wang, L., and Xia, X. (2020). Enhanced Performance of $LaFeO_3$ Perovskite for Peroxymonosulfate Activation Through Strontium Doping Towards 2,4-D Degradation. *Chem. Eng. J.* 384, 123377. doi:10.1016/j.cej.2019.123377

Clabel, H., J. L., Awan, I. T., Pinto, A. H., Nogueira, I. C., Bezzon, V. D. N., Leite, E. R., et al. (2020). Insights on the Mechanism of Solid State Reaction Between TiO_2 and $BaCO_3$ to Produce $BaTiO_3$ Powders: The Role of Calcination, Milling, and Mixing Solvent. *Ceramics Int.* 46, 2987–3001. doi:10.1016/j.ceramint.2019.09.296

Clabel H., J. L., Ferri, F. A., Zabotto, F. L., Rivera, V. A. G., Nogueira, I. C., Garcia, D., et al. (2016). Grain Size and Interfacial Interdiffusion Influence on the Magnetic and Dielectric Properties of Magnetoelectric $La_{0.7}Ba_{0.3}MnO_3$-$BaTiO_3$ Composites. *J. Magnetism Magn. Mater.* 407, 160–166. doi:10.1016/j.jmmm.2016.01.082

Clabel H., J. L., Awan, I. T., Rivera, V. A. G., Nogueira, I. C., Pereira-da-Silva, M. A., Li, M. S., et al. (2019). Growth Process and Grain Boundary Defects in Er Doped $BaTiO_3$ Processed by EB-PVD: A Study by XRD, FTIR, SEM and AFM. *Appl. Surf. Sci.* 493, 982–993. doi:10.1016/j.apsusc.2019.07.003

Clabel H., J. L., Nazrin, S. N., Lozano C., G., Pereira da Silva, M., Siu Li, M., and Marega Jr., E. (2021). Activation Energy and its Fluctuations at Grain Boundaries of Er3+:$BaTiO_3$ Perovskite Thin Films: Effect of Doping Concentration and Annealing Temperature. *Vacuum* 194, 110562. doi:10.1016/j.vacuum.2021.110562

Clabel H., J. L., Nicolodelli, G., Lozano C., G., G. Rivera, V. A., Ferreira, S. O., Pinto, A. H., et al. (2021). The Extrinsic Nature of Double Broadband Photoluminescence from the BaTiO3 Perovskite: Generation of White Light Emitters. *Phys. Chem. Chem. Phys.* 23, 18694–18706. doi:10.1039/d1cp01765a

Clabel H., J. L., Rivera, V. A. G., Nogueira, I. C., Leite, E. R., Pereira-da-Silva, M. A., Li, M. S., et al. (2017). Effects of Defects, Grain Size, and Thickness on the Optical Properties of $BaTiO_3$ Thin Films. *J. Lumin.* 192, 969–974. doi:10.1016/j.jlumin.2017.08.043

Clabel H., J. L., Zabotto, F. L., Nogueira, I. C., Schio, P., Garcia, D., De Lima, O. F., et al. (2014). Magnetoelectric Properties of Laminated $La_{0.7}Ba_{0.3}MnO_3$-$BaTiO_3$ Ceramic Composites. *J. Magnetism Magn. Mater.* 364, 18–23. doi:10.1016/j.jmmm.2014.04.014

Cohen, R. E. (1992). Origin of Ferroelectricity in Perovskite Oxides. *Nature* 358, 136–138. doi:10.1038/358136a0

Correa-Baena, J.-P., Saliba, M., Buonassisi, T., Grätzel, M., Abate, A., Tress, W., et al. (2017). Promises and Challenges of Perovskite Solar Cells. *Science* 358, 739–744. doi:10.1126/science.aam6323

Creutz, S. E., Crites, E. N., De Siena, M. C., and Gamelin, D. R. (2018). Colloidal Nanocrystals of Lead-Free Double-Perovskite (Elpasolite) Semiconductors: Synthesis and Anion Exchange to Access New Materials. *Nano Lett.* 18, 1118–1123. doi:10.1021/acs.nanolett.7b04659

Da Silva, L. F., Avansi, W., Andrés, J., Ribeiro, C., Moreira, M. L., Longo, E., et al. (2013). Long-Range and Short-Range Structures of Cube-Like Shape SrTiO3 Powders: Microwave-Assisted Hydrothermal Synthesis and Photocatalytic Activity. *Phys. Chem. Chem. Phys.* 15, 12386–12393. doi:10.1039/c3cp50643f

Ding, Q.-P., Yuan, Y.-P., Xiong, X., Li, R.-P., Huang, H.-B., Li, Z.-S., et al. (2008). Enhanced Photocatalytic Water Splitting Properties of $KNbO_3$ Nanowires Synthesized Through Hydrothermal Method. *J. Phys. Chem. C* 112, 18846–18848. doi:10.1021/jp8042768

Efros, A. (1982). Interband Light Absorption in Semiconductor Spheres. *Sov. Phys. Semicond.* 16, 772–775. Available at: https://www.researchgate.net/publication/279890805.

Fang, Y., Kong, X., Wang, D., Liu, J., and Cui, S. (2019). First Principle Calculations of Electronic, Band Structural, and Optical Properties of $Bi_xSr_{1-x}TiO_3$ Perovskite. *J. Phys. Chem. Sol.* 127, 107–114. doi:10.1016/j.jpcs.2018.11.023

Fenton, J. L., Steimle, B. C., and Schaak, R. E. (2018). Tunable Intraparticle Frameworks for Creating Complex Heterostructured Nanoparticle Libraries. *Science* 360, 513–517. doi:10.1126/science.aar5597

Fresno, F., Jana, P., Reñones, P., Coronado, J. M., Serrano, D. P., and de la Peña O'Shea, V. A. (2017). CO_2 Reduction over $NaNbO_3$ and $NaTaO_3$ Perovskite Photocatalysts. *Photochem. Photobiol. Sci.* 16, 17–23. doi:10.1039/c6pp00235h

Ghafoor, A., Bibi, I., Ata, S., Majid, F., Kamal, S., Iqbal, M., et al. (2021). Energy Band Gap Tuning of $LaNiO_3$ by Gd, Fe and Co Ions Doping to Enhance Solar Light Absorption for Efficient Photocatalytic Degradation of RhB Dye: A Mechanistic Approach. *J. Mol. Liquids* 343, 117581. doi:10.1016/j.molliq.2021.117581

Ghiasi, M., and Malekzadeh, A. (2014). Solar Photocatalytic Degradation of Methyl Orange Over $La_{0.7}Sr_{0.3}MnO_3$ Nano-Perovskite. *Sep. Purif. Tech.* 134, 12–19. doi:10.1016/j.seppur.2014.07.022

Golsdschmidt, V. V. M. (1962). Die gesetze der krystallochemie. *Naturwissenschaften, Naturwissenschaften.* 14, 477–485. doi:10.1177/089686089501500104

Gomathi Devi, L., and Krishnamurthy, G. (2009). TiO_2/$BaTiO_3$-Assisted Photocatalytic Mineralization of Diclofop-Methyl on UV-Light Irradiation in the Presence of Oxidizing Agents. *J. Hazard. Mater.* 162, 899–905. doi:10.1016/j.jhazmat.2008.05.116

Gómez-Solís, C., Oliva, J., Diaz-Torres, L. A., Bernal-Alvarado, J., Reyes-Zamudio, V., Abidov, A., et al. (2019). Efficient Photocatalytic Activity of $MSnO_3$ (M: Ca, Ba, Sr) Stannates for Photoreduction of 4-nitrophenol and Hydrogen Production Under UV Light Irradiation. *J. Photochem. Photobiol. A: Chem.* 371, 365–373. doi:10.1016/j.jphotochem.2018.11.039

Grabowska, E. (2016). Selected Perovskite Oxides: Characterization, Preparation and Photocatalytic Properties-A Review. *Appl. Catal. B: Environ.* 186, 97–126. doi:10.1016/j.apcatb.2015.12.035

Guleria, A., Sharma, R., Singh, A., Upadhyay, N. K., and Shandilya, P. (2021). Direct Dual-Z-Scheme PANI/Ag_2O/Cu_2O Heterojunction with Broad Absorption Range for Photocatalytic Degradation of Methylene Blue. *J. Water Process Eng.* 43, 102305. doi:10.1016/j.jwpe.2021.102305

Haron, W., Wisitsoraat, A., Sirimahachai, U., and Wongnawa, S. (2018). A Simple Synthesis and Characterization of $LaMo_3$ (M=Al, Co, Fe, Gd) Perovskites via Chemical Co-Precipitation Method. *Songklanakarin J. Sci. Technol.* 40, 484–491. doi:10.14456/sjst-psu.2018.64

Hemminger, J. C., Carr, R., and Somorjai, G. A. (1978). The Photoassisted Reaction of Gaseous Water and Carbon Dioxide Adsorbed on the $SrTiO_3$ (111) Crystal Face to Form Methane. *Chem. Phys. Lett.* 57, 100–104. doi:10.1016/0009-2614(78)80359-5

Hoefler, S. F., Trimmel, G., and Rath, T. (2017). Progress on Lead-Free Metal Halide Perovskites for Photovoltaic Applications: A Review. *Monatsh Chem.* 148, 795–826. doi:10.1007/s00706-017-1933-9

Hoffmann, M. R., Martin, S. T., Choi, W., and Bahnemann, D. W. (1995). Environmental Applications of Semiconductor Photocatalysis. *Chem. Rev.* 95, 69–96. doi:10.1021/cr00033a004

Hong, J., Zhang, W., Ren, J., and Xu, R. (2013). Photocatalytic Reduction of CO_2: A Brief Review on Product Analysis and Systematic Methods. *Anal. Methods* 5, 1086–1097. doi:10.1039/c2ay26270c

Hoshina, T. (2013). Size Effect of Barium Titanate: Fine Particles and Ceramics. *J. Ceram. Soc. Jpn.* 121, 156–161. doi:10.2109/jcersj2.121.156

Hsieh, P.-L., Naresh, G., Huang, Y.-S., Tsao, C.-W., Hsu, Y.-J., Chen, L.-J., et al. (2019). Shape-Tunable $SrTiO_3$ Crystals Revealing Facet-Dependent Optical and Photocatalytic Properties. *J. Phys. Chem. C* 123, 13664–13671. doi:10.1021/acs.jpcc.9b02081

Huang, H.-C., Yang, C.-L., Wang, M.-S., and Ma, X.-G. (2019). Chalcogens Doped $BaTiO_3$ for Visible Light Photocatalytic Hydrogen Production from Water Splitting. *Spectrochimica Acta A: Mol. Biomol. Spectrosc.* 208, 65–72. doi:10.1016/j.saa.2018.09.048

Humayun, M., Xu, L., Zhou, L., Zheng, Z., Fu, Q., and Luo, W. (2018). Exceptional Co-Catalyst Free Photocatalytic Activities of B and Fe Co-Doped $SrTiO_3$ for CO_2 Conversion and H_2 Evolution. *Nano Res.* 11, 6391–6404. doi:10.1007/s12274-018-2164-z

Hwang, J., Rao, R. R., Giordano, L., Katayama, Y., Yu, Y., and Shao-Horn, Y. (2017). Perovskites in Catalysis and Electrocatalysis. *Science* 358, 751–756. doi:10.1126/science.aam7092

Ibarra-Rodriguez, L. I., Huerta-Flores, A. M., Mora-Hernandez, J. M., and Torres-Martínez, L. M. (2020). Photocatalytic Evolution of H_2 Over Visible-Light Active $LaMO_3$ (M: Co, Mn, Fe) Perovskite Materials: Roles of Oxygenated Species in Catalytic Performance. *J. Phys. Chem. Sol.* 136, 109189. doi:10.1016/j.jpcs.2019.109189

Ismael, M., and Wark, M. (2019). Perovskite-Type $LaFeO_3$: Photoelectrochemical Properties and Photocatalytic Degradation of Organic Pollutants Under Visible Light Irradiation. *Catalysts* 9, 342. doi:10.3390/catal9040342

Jain, A., Ong, S. P., Hautier, G., Chen, W., Richards, W. D., Dacek, S., et al. (2013). Commentary: The Materials Project: A Materials Genome Approach to Accelerating Materials Innovation. *APL Mater.* 1, 011002. doi:10.1063/1.4812323

Kamat, P. V. (2012). Manipulation of Charge Transfer Across Semiconductor Interface. A Criterion that Cannot Be Ignored in Photocatalyst Design. *J. Phys. Chem. Lett.* 3, 663–672. doi:10.1021/jz201629p

Kanhere, P., Zheng, J., and Chen, Z. (2012). Visible Light Driven Photocatalytic Hydrogen Evolution and Photophysical Properties of Bi3+ Doped $NaTaO_3$. *Int. J. Hydrogen Energ.* 37, 4889–4896. doi:10.1016/j.ijhydene.2011.12.056

Karthikeyan, C., Arunachalam, P., Ramachandran, K., Al-Mayouf, A. M., and Karuppuchamy, S. (2020). Recent Advances in Semiconductor Metal Oxides with Enhanced Methods for Solar Photocatalytic Applications. *J. Alloys Comp.* 828, 154281. doi:10.1016/j.jallcom.2020.154281

Kirchartz, T., Márquez, J. A., Stolterfoht, M., and Unold, T. (2020). Photoluminescence-Based Characterization of Halide Perovskites for Photovoltaics. *Adv. Energ. Mater.* 10, 1904134. doi:10.1002/aenm.201904134

Kovalenko, M. V., Protesescu, L., and Bodnarchuk, M. I. (2017). Properties and Potential Optoelectronic Applications of Lead Halide Perovskite Nanocrystals. *Science* 358, 745–750. doi:10.1126/science.aam7093

Krückemeier, L., Krogmeier, B., Liu, Z., Rau, U., and Kirchartz, T. (2021). Understanding Transient Photoluminescence in Halide Perovskite Layer Stacks and Solar Cells. *Adv. Energ. Mater.* 11, 2003489. doi:10.1002/aenm.202003489

Kudo, A., and Miseki, Y. (2009). Heterogeneous Photocatalyst Materials for Water Splitting. *Chem. Soc. Rev.* 38, 253–278. doi:10.1039/b800489g

Kumar, A., Kumar, A., and Krishnan, V. (2020). Perovskite Oxide Based Materials for Energy and Environment-Oriented Photocatalysis. *ACS Catal.* 10, 10253–10315. doi:10.1021/acscatal.0c02947

Kumar, S., Sharma, M., Powar, S., Kabachkov, E. N., and Vaish, R. (2019). Impact of Remnant Surface Polarization on Photocatalytic and Antibacterial Performance of $BaTiO_3$. *J. Eur. Ceram. Soc.* 39, 2915–2922. doi:10.1016/j.jeurceramsoc.2019.03.029

Kurbakov, A. I. (2010). Electronic, Structural and Magnetic Phase Diagram of $Sm_{1-x}SrxMnO_3$ Manganites. *J. Magnetism Magn. Mater.* 322, 967–972. doi:10.1016/j.jmmm.2009.11.034

Letifi, H., Dridi, D., Litaiem, Y., Ammar, S., Dimassi, W., and Chtourou, R. (2021). High Efficient and Cost Effective Titanium Doped Tin Dioxide Based Photocatalysts Synthesized via Co-Precipitation Approach. *Catalysts* 11, 803. doi:10.3390/catal11070803

Li, C., Lu, X., Ding, W., Feng, L., Gao, Y., and Guo, Z. (2008). Formability of ABX_3 (X = F, Cl, Br, I) Halide Perovskites. *Acta Crystallogr. Sect. B* 64, 702–707. doi:10.1107/S0108768108032734

Li, D., Ouyang, S., Xu, H., Lu, D., Zhao, M., Zhang, X., et al. (2016). Synergistic Effect of Au and Rh on $SrTiO_3$ in Significantly Promoting Visible-Light-Driven Syngas Production from CO_2 and H_2O. *Chem. Commun.* 52, 5989–5992. doi:10.1039/c6cc00836d

Li, M., Begum, R., Fu, J., Xu, Q., Koh, T. M., Veldhuis, S. A., et al. (2018). Low Threshold and Efficient Multiple Exciton Generation in Halide Perovskite Nanocrystals. *Nat. Commun.* 919, 1–7. doi:10.1038/s41467-018-06596-1

Li, M., and Li, J. C. (2006). Size Effects on the Band-Gap of Semiconductor Compounds. *Mater. Lett.* 60, 2526–2529. doi:10.1016/j.matlet.2006.01.032

Li, N., Tao, S., Chen, Y., Niu, X., Onwudinanti, C. K., Hu, C., et al. (2019). Cation and Anion Immobilization Through Chemical Bonding Enhancement with Fluorides for Stable Halide Perovskite Solar Cells. *Nat. Energ.* 4, 408–415. doi:10.1038/s41560-019-0382-6

Liang, J., Chen, D., Yao, X., Zhang, K., Qu, F., Qin, L., et al. (2020). Recent Progress and Development in Inorganic Halide Perovskite Quantum Dots for Photoelectrochemical Applications. *Small* 16, 1903398. doi:10.1002/SMLL.201903398

Liu, B., and Zhao, X. (2010). A Kinetic Model for Evaluating the Dependence of the Quantum Yield of Nano-TiO_2 Based Photocatalysis on Light Intensity, Grain Size, Carrier Lifetime, and Minority Carrier Diffusion Coefficient: Indirect Interfacial Charge Transfer. *Electrochimica Acta* 55, 4062–4070. doi:10.1016/j.electacta.2010.01.087

Liu, J., Liu, L., Zhang, J., Jin, L., Wang, D., Wei, J., et al. (2020). Charge Effects in Donor-Doped Perovskite Ferroelectrics. *J. Am. Ceram. Soc.* 103, 5392–5399. doi:10.1111/jace.17270

Liu, K., Mi, L., Wang, H., Xiong, X., Zhang, K., and Wang, B. (2021). Preparation of $Ba_{1-x}Sr_xTiO_3$ by the Sol-Gel Assisted Solid Phase Method: Study on its Formation Mechanism and Photocatalytic Hydrogen Production Performance. *Ceramics Int.* 47, 22055–22064. doi:10.1016/j.ceramint.2021.04.226

Liu, L., Zhao, R., Xiao, C., Zhang, F., Pevere, F., Shi, K., et al. (2019). Size-Dependent Phase Transition in Perovskite Nanocrystals. *J. Phys. Chem. Lett.* 10, 5451–5457. doi:10.1021/acs.jpclett.9b02058

Liu, S., Wang, J., Shen, B., Zhai, J., Hao, H., and Zhao, L. (2017). Poly(vinylidene Fluoride) Nanocomposites with a Small Loading of Core-Shell Structured $BaTiO_3$@Al_2O_3 Nanofibers Exhibiting High Discharged Energy Density and Efficiency. *J. Alloys Comp.* 696, 136–142. doi:10.1016/j.jallcom.2016.11.186

Liu, X., Xiao, L., Zhang, Y., and Sun, H. (2020). Significantly Enhanced Piezo-Photocatalytic Capability in $BaTiO_3$ Nanowires for Degrading Organic Dye. *J. Materiomics* 6, 256–262. doi:10.1016/j.jmat.2020.03.004

Loiudice, A., Strach, M., Saris, S., Chernyshov, D., and Buonsanti, R. (2019). Universal Oxide Shell Growth Enables *In Situ* Structural Studies of Perovskite Nanocrystals During the Anion Exchange Reaction. *J. Am. Chem. Soc.* 141, 8254–8263. doi:10.1021/jacs.9b02061

Lu, C.-H., Biesold-Mcgee, G. V., Liu, Y., Kang, Z., and Lin, Z. (2020). Doping and Ion Substitution in Colloidal Metal Halide Perovskite Nanocrystals. *Chem. Soc. Rev.* 49, 4953–5007. doi:10.1039/c9cs00790c

Lu, S., Wang, G., Chen, S., Yu, H., Ye, F., and Quan, X. (2018). Heterogeneous Activation of Peroxymonosulfate by $LaCo_{1-x}Cu_xO_3$ Perovskites for Degradation of Organic Pollutants. *J. Hazard. Mater.* 353, 401–409. doi:10.1016/j.jhazmat.2018.04.021

Machida, M., Miyazaki, K., Matsushima, S., and Arai, M. (2003). Photocatalytic Properties of Layered Perovskite Tantalates, $MLnTa_2O_7$ (M = Cs, Rb, Na, and H; Ln = La, Pr, Nd, and Sm). *J. Mater. Chem.* 13, 1433–1437. doi:10.1039/b301938c

Maeda, K., and Domen, K. (2007). New Non-Oxide Photocatalysts Designed for Overall Water Splitting Under Visible Light. *J. Phys. Chem. C* 111, 7851–7861. doi:10.1016/S1380-7323(06)80014-210.1021/jp070911w

Marszewski, M., Cao, S., Yu, J., and Jaroniec, M. (2015). Semiconductor-Based Photocatalytic CO_2 Conversion. *Mater. Horiz.* 2, 261–278. doi:10.1039/c4mh00176a

Meng, J., Lan, Z., Lin, Q., Chen, T., Chen, X., Wei, X., et al. (2019). Cubic-Like $BaZrO_3$ Nanocrystals with Exposed {001}/{011} Facets and Tuned Electronic Band Structure for Enhanced Photocatalytic Hydrogen Production. *J. Mater. Sci.* 54, 1967–1976. doi:10.1007/s10853-018-2995-8

Miao, J., Duan, X., Li, J., Dai, J., Liu, B., Wang, S., et al. (2019). Boosting Performance of Lanthanide Magnetism Perovskite for Advanced Oxidation Through Lattice Doping with Catalytically Inert Element. *Chem. Eng. J.* 355, 721–730. doi:10.1016/j.cej.2018.08.192

Miao, J., Sunarso, J., Su, C., Zhou, W., Wang, S., and Shao, Z. (2017). $SrCo_{1-x}Ti_xO_3$–δ Perovskites as Excellent Catalysts for Fast Degradation of Water Contaminants in Neutral and Alkaline Solutions. *Sci. Rep.* 7, 1–10. doi:10.1038/srep44215

Modak, B., Srinivasu, K., and Ghosh, S. K. (2014). Photocatalytic Activity of $NaTaO_3$ Doped with N, Mo, and (N,Mo): A Hybrid Density Functional Study. *J. Phys. Chem. C* 118, 10711–10719. doi:10.1021/jp410995g

Mott, N. F. (1968). Conduction in Glasses Containing Transition Metal Ions. *J. Non-Crystalline Sol.* 1, 1–17. doi:10.1016/0022-3093(68)90002-1

Odling, G., and Robertson, N. (2019). Bridging the Gap Between Laboratory and Application in Photocatalytic Water Purification. *Catal. Sci. Technol.* 9, 533–545. doi:10.1039/c8cy02438c

Oksenberg, E., Merdasa, A., Houben, L., Kaplan-Ashiri, I., Rothman, A., Scheblykin, I. G., et al. (2020). Large Lattice Distortions and Size-Dependent Bandgap Modulation in Epitaxial Halide Perovskite Nanowires. *Nat. Commun.* 11, 1–11. doi:10.1038/s41467-020-14365-2

Osterloh, F. E. (2008). Inorganic Materials as Catalysts for Photochemical Splitting of Water. *Chem. Mater.* 20, 35–54. doi:10.1021/cm7024203

Ou, Q., Bao, X., Zhang, Y., Shao, H., Xing, G., Li, X., et al. (2019). Band Structure Engineering in Metal Halide Perovskite Nanostructures for Optoelectronic Applications. *Nano Mater. Sci.* 1, 268–287. doi:10.1016/j.nanoms.2019.10.004

Palstra, T. T. M., Batlogg, B., Van Dover, R. B., Schneemeyer, L. F., and Waszczak, J. V. (1990). Dissipative Flux Motion in High-Temperature Superconductors. *Phys. Rev. B* 41, 6621–6632. doi:10.1103/PhysRevB.41.6621

Parida, K. M., Reddy, K. H., Martha, S., Das, D. P., and Biswal, N. (2010). Fabrication of Nanocrystalline $LaFeO_3$: An Efficient Sol-Gel Auto-Combustion Assisted Visible Light Responsive Photocatalyst for Water Decomposition. *Int. J. Hydrogen. Energ.* 35, 12161–12168. doi:10.1016/j.ijhydene.2010.08.029

Park, K.-W., and Kolpak, A. M. (2019). Optimal Methodology for Explicit Solvation Prediction of Band Edges of Transition Metal Oxide Photocatalysts. *Commun. Chem.* 2, 79. doi:10.1038/s42004-019-0179-3

Park, Y.-U., Bai, J., Wang, L., Yoon, G., Zhang, W., Kim, H., et al. (2017). *In Situ* Tracking Kinetic Pathways of Li+/Na+ Substitution During Ion-Exchange Synthesis of $Li_xNa_{1.5-x}VOPO_4F_{0.5}$. *J. Am. Chem. Soc.* 139, 12504–12516. doi:10.1021/jacs.7b05302

Patel, M., Kumar, R., Kishor, K., Mlsna, T., Pittman, C. U., and Mohan, D. (2019). Pharmaceuticals of Emerging Concern in Aquatic Systems: Chemistry, Occurrence, Effects, and Removal Methods. *Chem. Rev.* 119, 3510–3673. doi:10.1021/acs.chemrev.8b00299

Patil, M. S., Kitchamsetti, N., Mulani, S. R., Rondiya, S. R., Deshpande, N. G., Patil, R. A., et al. (2021). Photocatalytic Behavior of $Ba(Sb/Ta)_2O_6$ Perovskite for Reduction of Organic Pollutants: Experimental and DFT Correlation. *J. Taiwan Inst. Chem. Eng.* 122, 201–209. doi:10.1016/j.jtice.2021.04.032

Pellegrini, G., Mattei, G., and Mazzoldi, P. (2005). Finite Depth Square Well Model: Applicability and Limitations. *J. Appl. Phys.* 97, 073706. doi:10.1063/1.1868875

Peoples, J., Li, X., Lv, Y., Qiu, J., Huang, Z., and Ruan, X. (2019). A Strategy of Hierarchical Particle Sizes in Nanoparticle Composite for Enhancing Solar Reflection. *Int. J. Heat Mass Transfer* 131, 487–494. doi:10.1016/j.ijheatmasstransfer.2018.11.059

Protesescu, L., Yakunin, S., Nazarenko, O., Dirin, D. N., and Kovalenko, M. V. (2018). Low-Cost Synthesis of Highly Luminescent Colloidal Lead Halide Perovskite Nanocrystals by Wet Ball Milling. *ACS Appl. Nano Mater.* 1, 1300–1308. doi:10.1021/acsanm.8b00038

Qi, W. H. (2005). Size Effect on Melting Temperature of Nanosolids. *Physica B: Condensed Matter* 368, 46–50. doi:10.1016/j.physb.2005.06.035

Qi, W. H., and Wang, M. P. (2004). Size and Shape Dependent Melting Temperature of Metallic Nanoparticles. *Mater. Chem. Phys.* 88, 280–284. doi:10.1016/j.matchemphys.2004.04.026

Ramakanth, S., and James Raju, K. C. (2014). Band Gap Narrowing in $BaTiO_3$ Nanoparticles Facilitated by Multiple Mechanisms. *J. Appl. Phys.* 115, 173507–7. doi:10.1063/1.4871776

Rao, M. P., Nandhini, V. P., Wu, J. J., Syed, A., Ameen, F., and Anandan, S. (2018). Synthesis of N-Doped Potassium Tantalate Perovskite Material for Environmental Applications. *J. Solid State. Chem.* 258, 647–655. doi:10.1016/j.jssc.2017.11.031

Ravi, V. K., Markad, G. B., and Nag, A. (2016). Band Edge Energies and Excitonic Transition Probabilities of Colloidal $CsPbX_3$ (X = Cl, Br, I) Perovskite Nanocrystals. *ACS Energ. Lett.* 1, 665–671. doi:10.1021/acsenergylett.6b00337

Ravi, V. K., Saikia, S., Yadav, S., Nawale, V. V., and Nag, A. (2020). $CsPbBr_3$/ZnS Core/Shell Type Nanocrystals for Enhancing Luminescence Lifetime and Water Stability. *ACS Energ. Lett.* 5, 1794–1796. doi:10.1021/acsenergylett.0c00858

Reid, A. J., Carlson, A. K., Creed, I. F., Eliason, E. J., Gell, P. A., Johnson, P. T. J., et al. (2019). Emerging Threats and Persistent Conservation Challenges for Freshwater Biodiversity. *Biol. Rev.* 94, 849–873. doi:10.1111/brv.12480

Rekavandi, N., Malekzadeh, A., and Ghiasi, E. (2019). Methyl Orange Degradation Using Nano-$LaMnO_3$ as a Green Catalyst Under the Mild Conditions. *Nanochem. Res.* 4, 1–10. doi:10.22036/ncr.2019.01.001

Romani, L., and Malavasi, L. (2020). Solar-Driven Hydrogen Generation by Metal Halide Perovskites: Materials, Approaches, and Mechanistic View. *ACS Omega* 5, 25511–25519. doi:10.1021/acsomega.0c03829

Rose, J. H., Ferrante, J., and Smith, J. R. (1981). Universal Binding Energy Curves for Metals and Bimetallic Interfaces. *Phys. Rev. Lett.* 47, 675–678. doi:10.1103/PhysRevLett.47.675

Roy, N., and Chakraborty, S. (2021). ZnO as Photocatalyst: An Approach to Waste Water Treatment. *Mater. Today Proc.* 46, 6399–6403. doi:10.1016/j.matpr.2020.06.264

Saparov, B., and Mitzi, D. B. (2016). Organic-Inorganic Perovskites: Structural Versatility for Functional Materials Design. *Chem. Rev.* 116, 4558–4596. doi:10.1021/acs.chemrev.5b00715

Sapra, S., and Sarma, D. D. (2004). Evolution of the Electronic Structure with Size in II-VI Semiconductor Nanocrystals. *Phys. Rev. B* 69, 1–7. doi:10.1103/PhysRevB.69.125304

Schanze, K. S., Kamat, P. V., Yang, P., and Bisquert, J. (2020). Progress in Perovskite Photocatalysis. *ACS Energ. Lett.* 5, 2602–2604. doi:10.1021/acsenergylett.0c01480

Schilling, C., Ganduglia-Pirovano, M. V., and Hess, C. (2018). Experimental and Theoretical Study on the Nature of Adsorbed Oxygen Species on Shaped Ceria Nanoparticles. *J. Phys. Chem. Lett.* 9, 6593–6598. doi:10.1021/acs.jpclett.8b02728

Serpone, N., Lawless, D., Khairutdinov, R., and Pelizzetti, E. (1995). Subnanosecond Relaxation Dynamics in TiO_2 Colloidal Sols (Particle Sizes Rp = 1.0-13.4 Nm). Relevance to Heterogeneous Photocatalysis. *J. Phys. Chem.* 99, 16655–16661. doi:10.1021/j100045a027

Sheng, J., He, Y., Li, J., Yuan, C., Huang, H., Wang, S., et al. (2020). Identification of Halogen-Associated Active Sites on Bismuth-Based Perovskite Quantum Dots for Efficient and Selective CO_2-to-CO Photoreduction. *ACS Nano* 14, 13103–13114. doi:10.1021/acsnano.0c04659

Shi, H., and Zou, Z. (2012). Photophysical and Photocatalytic Properties of $ANbO_3$ (A=Na, K) Photocatalysts. *J. Phys. Chem. Sol.* 73, 788–792. doi:10.1016/j.jpcs.2012.01.026

Shi, R., Waterhouse, G. I. N., and Zhang, T. (2017). Recent Progress in Photocatalytic CO_2 Reduction over Perovskite Oxides. *Sol. RRL* 1, 1700126. doi:10.1002/solr.201700126

Shyamal, S., Dutta, S. K., Das, T., Sen, S., Chakraborty, S., and Pradhan, N. (2020). Facets and Defects in Perovskite Nanocrystals for Photocatalytic CO_2 Reduction. *J. Phys. Chem. Lett.* 11, 3608–3614. doi:10.1021/acs.jpclett.0c01088

Sieland, F., Schneider, J., and Bahnemann, D. W. (2018). Photocatalytic Activity and Charge Carrier Dynamics of TiO_2 Powders with a Binary Particle Size Distribution. *Phys. Chem. Chem. Phys.* 20, 8119–8132. doi:10.1039/c8cp00398j

Singh, S., Chen, H., Shahrokhi, S., Wang, L. P., Lin, C.-H., Hu, L., et al. (2020). Hybrid Organic-Inorganic Materials and Composites for Photoelectrochemical Water Splitting. *ACS Energ. Lett.* 5, 1487–1497. doi:10.1021/acsenergylett.0c00327

Slavney, A. H., Hu, T., Lindenberg, A. M., and Karunadasa, H. I. (2016). A Bismuth-Halide Double Perovskite with Long Carrier Recombination Lifetime for Photovoltaic Applications. *J. Am. Chem. Soc.* 138, 2138–2141. doi:10.1021/jacs.5b13294

Soltani, T., Tayyebi, A., and Lee, B.-K. (2018). Quick and Enhanced Degradation of Bisphenol A by Activation of Potassium Peroxymonosulfate to SO_{4-} with Mn-Doped $BiFeO_3$ Nanoparticles as a Heterogeneous Fenton-Like Catalyst. *Appl. Surf. Sci.* 441, 853–861. doi:10.1016/j.apsusc.2018.02.063

Takasugi, S., Tomita, K., Iwaoka, M., Kato, H., and Kakihana, M. (2015). The Hydrothermal and Solvothermal Synthesis of $LiTaO_3$ Photocatalyst: Suppressing the Deterioration of the Water Splitting Activity Without Using a Cocatalyst. *Int. J. Hydrogen Energ.* 40, 5638–5643. doi:10.1016/j.ijhydene.2015.02.121

Tang, C., Chen, C., Xu, W., and Xu, L. (2019). Design of Doped Cesium Lead Halide Perovskite as a Photo-Catalytic CO_2 Reduction Catalyst. *J. Mater. Chem. A.* 7, 6911–6919. doi:10.1039/c9ta00550a

Tang, J., Durrant, J. R., and Klug, D. R. (2008). Mechanism of Photocatalytic Water Splitting in TiO_2. Reaction of Water with Photoholes, Importance of Charge Carrier Dynamics, and Evidence for Four-Hole Chemistry. *J. Am. Chem. Soc.* 130, 13885–13891. doi:10.1021/ja8034637

Tasleem, S., and Tahir, M. (2020). Recent Progress in Structural Development and Band Engineering of Perovskites Materials for Photocatalytic Solar Hydrogen Production: A Review. *Int. J. Hydrogen. Energ.* 45, 19078–19111. doi:10.1016/j.ijhydene.2020.05.090

Tauc, J., and Menth, A. (1972). States in the Gap. *J. Non-Crystalline Sol.* 8-10, 569–585. doi:10.1016/0022-3093(72)90194-9

Toshniwal, A., and Kheraj, V. (2017). Development of Organic-Inorganic Tin Halide Perovskites: A Review. *Solar Energy* 149, 54–59. doi:10.1016/j.solener.2017.03.077

Volonakis, G., and Giustino, F. (2018). Surface Properties of Lead-Free Halide Double Perovskites: Possible Visible-Light Photo-Catalysts for Water Splitting. *Appl. Phys. Lett.* 112, 243901. doi:10.1063/1.5035274

Walter, M. G., Warren, E. L., McKone, J. R., Boettcher, S. W., Mi, Q., Santori, E. A., et al. (2010). Solar Water Splitting Cells. *Chem. Rev.* 110, 6446–6473. doi:10.1021/cr1002326

Wang, M., Fang, M., Min, X., Huang, Z., Tang, C., Liu, Y. g., et al. (2017). Molten Salt Synthesis of $NaNb_xTa_{1-x}O_3$ Perovskites with Enhanced Photocatalytic Activity. *Chem. Phys. Lett.* 686, 18–25. doi:10.1016/j.cplett.2017.08.029

Wang, R., Zhu, Y., Qiu, Y., Leung, C.-F., He, J., Liu, G., et al. (2013). Synthesis of Nitrogen-Doped $KNbO_3$ Nanocubes with High Photocatalytic Activity for Water Splitting and Degradation of Organic Pollutants Under Visible Light. *Chem. Eng. J.* 226, 123–130. doi:10.1016/j.cej.2013.04.049

Wang, W., Xu, X., Zhou, W., and Shao, Z. (2017). Recent Progress in Metal-Organic Frameworks for Applications in Electrocatalytic and Photocatalytic Water Splitting. *Adv. Sci.* 4, 1600371. doi:10.1002/advs.201600371

Wang, Y., Wang, L., Liu, R., and Li, X. (2019). Casein Templated Synthesis of Porous Perovskite and its Application in Visible-Light Photocatalytic Degradation of Methylene Blue. *Mater. Sci. Semiconductor Process.* 103, 104597. doi:10.1016/j.mssp.2019.104597

Wood, A., Giersig, M., and Mulvaney, P. (2001). Fermi Level Equilibration in Quantum Dot–Metal Nanojunctions. *J. Phys. Chem. B* 105, 8810–8815. doi:10.1021/jp011576t

Wu, D., Zhao, X., Huang, Y., Lai, J., Li, H., Yang, J., et al. (2021). Lead-Free Perovskite Cs_2AgBiX_6 Nanocrystals with a Band Gap Funnel Structure for Photocatalytic CO_2 Reduction Under Visible Light. *Chem. Mater.* 33, 4971–4976. doi:10.1021/acs.chemmater.1c00753

Wu, X., Yin, S., Dong, Q., and Sato, T. (2013). Preparation and Visible Light Induced Photocatalytic Activity of C-$NaTaO_3$ and C-$NaTaO_3$-Cl-TiO_2 Composite. *Phys. Chem. Chem. Phys.* 15, 20633–20640. doi:10.1039/c3cp53437e

Wu, Y., Chen, W., Chen, G., Liu, L., He, Z., and Liu, R. (2018). The Impact of Hybrid Compositional Film/Structure on Organic-Inorganic Perovskite Solar Cells. *Nanomaterials* 8, 1–27. doi:10.3390/nano8060356

Xia, Y., Zhang, L., Hu, B., Yu, J., Al-Ghamdi, A. A., and Wageh, S. (2021). Design of Highly-Active Photocatalytic Materials for Solar Fuel Production. *Chem. Eng. J.* 421, 127732. doi:10.1016/j.cej.2020.127732

Xiao, H., Liu, P., Wang, W., Ran, R., Zhou, W., and Shao, Z. (2020). Ruddlesden–Popper Perovskite Oxides for Photocatalysis-Based Water Splitting and Wastewater Treatment. *Energy Fuels.* 34, 9208–9221. doi:10.1021/acs.energyfuels.0c02301

Xu, Y.-F., Yang, M.-Z., Chen, B.-X., Wang, X.-D., Chen, H.-Y., Kuang, D.-B., et al. (2017). A $CsPbBr_3$ Perovskite Quantum Dot/Graphene Oxide Composite for Photocatalytic CO_2 Reduction. *J. Am. Chem. Soc.* 139, 5660–5663. doi:10.1021/jacs.7b00489

Yan, Y., Yang, H., Zhao, X., Li, R., and Wang, X. (2018). Enhanced Photocatalytic Activity of Surface Disorder-Engineered $CaTiO_3$. *Mater. Res. Bull.* 105, 286–290. doi:10.1016/j.materresbull.2018.05.008

Yang, C.-K., Yamazaki, Y., Aydin, A., and Haile, S. M. (2014). Thermodynamic and Kinetic Assessments of Strontium-Doped Lanthanum Manganite Perovskites for Two-Step Thermochemical Water Splitting. *J. Mater. Chem. A.* 2, 13612–13623. doi:10.1039/c4ta02694b

Yang, W. S., Noh, J. H., Jeon, N. J., Kim, Y. C., Ryu, S., Seo, J., et al. (2015). High-Performance Photovoltaic Perovskite Layers Fabricated Through Intramolecular Exchange. *Science* 348, 1234–1237. doi:10.1126/science.aaa9272

Yang, Y., Kang, L., and Li, H. (2019). Enhancement of Photocatalytic Hydrogen Production of $BiFeO_3$ by Gd3+ Doping. *Ceramics Int.* 45, 8017–8022. doi:10.1016/j.ceramint.2018.12.150

Yousif, N., and Gurjar, B. R. (2018). "Water Pollution, Human Health and Remediation," in *Water Remediat. Energy, Environ. Sustain.*, 1–50. doi:10.1016/j.neuropsychologia.2015.07.010%0A

Yu, H., Ouyang, S., Yan, S., Li, Z., Yu, T., and Zou, Z. (2011). Sol-Gel Hydrothermal Synthesis of Visible-Light-Driven Cr-Doped $SrTiO_3$ for Efficient Hydrogen Production. *J. Mater. Chem.* 21, 11347–11351. doi:10.1039/c1jm11385b

Zanatta, A. R. (2019). Revisiting the Optical Bandgap of Semiconductors and the Proposal of a Unified Methodology to its Determination. *Sci. Rep.* 9, 11225. doi:10.1038/s41598-019-47670-y

Zhang, G., Liu, G., Wang, L., and Irvine, J. T. S. (2016). Inorganic Perovskite Photocatalysts for Solar Energy Utilization. *Chem. Soc. Rev.* 45, 5951–5984. doi:10.1039/c5cs00769k

Zhang, L., Nie, Y., Hu, C., and Qu, J. (2012). Enhanced Fenton Degradation of Rhodamine B Over Nanoscaled Cu-Doped $LaTiO_3$ Perovskite. *Appl. Catal. B: Environ.* 125, 418–424. doi:10.1016/j.apcatb.2012.06.015

Zhu, Y., Zhang, L., Zhao, B., Chen, H., Liu, X., Zhao, R., et al. (2019). Improving the Activity for Oxygen Evolution Reaction by Tailoring Oxygen Defects in Double Perovskite Oxides. *Adv. Funct. Mater.* 29, 1–12. doi:10.1002/adfm.201901783

Conflict of Interest: The authors declare that the research was conducted in the absence of any commercial or financial relationships that could be construed as a potential conflict of interest.

The handling editor declared a past co-authorship with one of the authors JLCH.

Publisher's Note: All claims expressed in this article are solely those of the authors and do not necessarily represent those of their affiliated organizations, or those of the publisher, the editors, and the reviewers. Any product that may be evaluated in this article, or claim that may be made by its manufacturer, is not guaranteed or endorsed by the publisher.

Copyright © 2022 Clabel H., Chacaliaza-Ricaldi and Marega Jr. This is an open-access article distributed under the terms of the Creative Commons Attribution License (CC BY). The use, distribution or reproduction in other forums is permitted, provided the original author(s) and the copyright owner(s) are credited and that the original publication in this journal is cited, in accordance with accepted academic practice. No use, distribution or reproduction is permitted which does not comply with these terms.